Research Article

ADVANCED PHOTONICS

Uniform-velocity spacetime crystals

Zoé-Lise Deck-Léger,[a,*] Nima Chamanara,[a] Maksim Skorobogatiy,[b] Mário G. Silveirinha,[c] and Christophe Caloz[a]

[a]Polytechnique Montréal, Department of Electrical Engineering, Montréal, Quebec, Canada
[b]Polytechnique Montréal, Department of Engineering Physics, Montréal, Quebec, Canada
[c]Universidade de Lisboa - Instituto Superior Técnico and Instituto de Telecomunicações, Department of Electrical Engineering, Lisbon, Portugal

Abstract. We perform a comprehensive analysis of uniform-velocity bilayer spacetime crystals, combining concepts of conventional photonic crystals and special relativity. Given that a spacetime crystal consists of a sequence of spacetime discontinuities, we do this by solving the following sequence of problems: (1) the spacetime interface, (2) the double spacetime interface, or spacetime slab, (3) the unbounded crystal, and (4) the truncated crystal. For these problems, we present the following results: (1) an extension of the Stokes principle to spacetime interfaces, (2) an interference-based analysis of the interference phenomenology, (3) a quick linear approximation of the dispersion diagrams, a description of simultaneous wavenumber and frequency bandgaps, and (4) the explanation of the effects of different types of spacetime crystal truncations and the corresponding scattering coefficients. This work may constitute the foundation for a virtually unlimited number of novel canonical spacetime media and metamaterial problems.

Keywords: crystals; special relativity; Lorentz transformations; spacetime; bandgap structures.

Received Aug. 12, 2019; accepted for publication Oct. 8, 2019; published online Oct. 31, 2019.

© The Authors. Published by SPIE and CLP under a Creative Commons Attribution 4.0 Unported License. Distribution or reproduction of this work in whole or in part requires full attribution of the original publication, including its DOI.

[DOI: 10.1117/1.AP.1.5.056002]

1 Introduction

Crystals are structures that are periodic, either at the atomic level (e.g., electronic crystals)[1] or at the supermolecular level of artificial scatterers (e.g., photonic crystals).[2] Their periodicity confers them a dispersion in the form of a bandgap structure, which leads to spatiotemporal filtering. They have a myriad of applications, such as for instance x-ray imaging[3] and Bragg gratings[4] in the case of electromagnetics.

In conventional crystals, the periodicity is purely spatial: the structure is composed of a one-, two-, or three-dimensional (1-, 2-, or 3-D) lattice of molecules or artificial particles, which may be seen as a variation of medium parameters in space. Medium variation may also occur in time and a periodic time variation leads then to time crystals. Time crystals were first studied in the 1960s under the form of temporally modulated 1-D structures, whose controlled instabilities led to parametric amplifiers[5,6] and whose asymmetric frequency transitions led to nonreciprocal devices.[7,8] Such time crystals,[9–13] and more generally time-varying structures,[14–16] have recently experienced a renewed attention. Moreover, the concept of spontaneous time crystals, which are time crystals produced by a nonperiodic stimulus, was introduced as a new state of matter.[17]

In general, medium variation may occur in both space and time, and a periodic spacetime variation leads to spacetime crystals, supporting extremely rich and largely unexplored physics. Spacetime crystals may be moving-medium structures[18–21] or modulated-medium structures, the former involving the motion of matter, and the latter involving the motion of a perturbation. The two share much of the same physics, including Doppler-like frequency transitions,[22] amplification,[23,24] and Bradley-aberration deflections.[25] Modulated structures are easier to realize,[26] more practical, and more diverse, as they may be superluminal, i.e., faster than the speed of light, have multiple periods, and accelerate without the application of any force.[27] For these reasons, this paper focuses on modulated structures while comparing them with moving structures whenever appropriate.

Spacetime crystals may generally include the three dimensions of space and the single dimension of time and are hence $(3+1)$-D. In this paper, the quantitative developments are restricted to a single dimension of space, corresponding to $(1+1)$-D crystals, but the qualitative concepts equally apply to $(1, 2, 3+1)$-D spacetime crystals.

Figure 1 represents two canonical spacetime crystals in spacetime diagrams, where z and t denote space and time,

*Address all correspondence to Zoé-Lise Deck-Léger, E-mail: zoe-lise.deck-leger@polymtl.ca

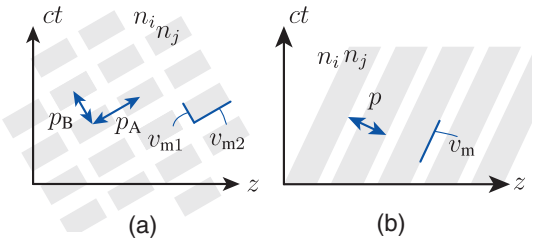

Fig. 1 Representation of two canonical spacetime crystals. Here, the variable z is intended to represent the hyperspace, i.e., the three dimensions of space. The white and gray regions correspond to media with refractive indices n_i and n_j, respectively. (a) Double-period (p_A and p_B) structure, characterized by two velocities, v_{m1} and v_{m2}, which may be interpreted as acceleration at the corner. (b) Single-period (p) structure, characterized by a unique and uniform velocity, v_m.

and c is the speed of light in free space. For simplicity, throughout the paper, we consider crystals composed of just two homogeneous media with refractive indices n_i and n_j separated by sharp, step discontinuities. The first crystal type, represented in Fig. 1(a), is a multiple-periodicity structure [two periods in the $(1+1)$-D rectangular-scatterer case]. Such multiple-periodicity, which may involve up to four periods (three spatial and one temporal) in the $(3+1)$-D case, requires the presence of different slopes in the spacetime diagram, and hence multiple velocities. The set of velocities may be discrete (e.g., two velocities in the figure) or continuous (e.g., as obtained by rounding the corners of the gray areas in the figure). Some of the features of such crystals may be studied using spacetime ray tracing.[28–32]

The second crystal type, shown in Fig. 1(b), is a single-periodicity structure, featuring perturbation that moves along the z axis with a single and uniform velocity. Such uniform-velocity modulated spacetime crystals have been investigated under the form of traveling-wave amplifiers,[33–35] and, more recently, under various forms for magnetless nonreciprocity.[36–41] This paper focuses on this type of spacetime crystal because of its greater simplicity, and because this fundamental problem already exhibits unreported and interesting physics. Since a crystal consists of a periodic sequence of medium discontinuities, we devote a considerable amount of time to the study of spacetime interfaces corresponding to such discontinuities.

This work studies the scattering of waves from uniform-velocity spacetime crystals [Fig. 1(b)] by generalizing standard crystallography and leveraging special relativity. It retrieves the known dispersion diagrams[42,43] and transfer-matrix results[44] and presents a number of new results, including the generalization of the Stokes principle for spacetime interfaces, the derivation of the interference condition in spacetime slabs, and a complete description of the dispersion diagrams of spacetime crystals, with the identification and explanation of dispersion-slope asymmetry, the demonstration of simultaneous frequency and wavenumber bandgaps, and the analytical derivation of the bandgap positions. The calculation of the scattered-wave amplitudes for finite crystals is also provided.

The paper is organized as follows. Section 2 presents preliminary concepts and principles, including the description of a spacetime interface, the introduction of generalized spacetime diagrams, the distinction of three velocity regimes in spacetime structures, our strategy to compute the fields scattered by spacetime structures, a brief recall on Lorentz transformations, the proper selection of Lorentz frames for subluminal and superluminal structures, and a discussion on the duality existing between space and time in spacetime systems. Section 3 deals with a single interface of a spacetime crystal, deriving its scattering coefficients, its frequency transitions, and generalizing the Stokes relations. Section 4 solves the double-interface problem of a spacetime slab, describing its scattering phenomenology, deriving its frequency transitions, phase shifts, and scattering coefficients, and graphically illustrates the gap interference condition. Section 5 studies an unbounded bilayer crystal. It develops a linear approximation of the dispersion diagram, finds the position of the centers of the bandgaps, derives the transfer matrix for a unit cell of a spacetime crystal, subsequently computes the dispersion relation, and explains its spacetime specifics in terms of the Brillouin zone, the complex bandgaps, and the bandgap edges. Section 6 uses the previously derived unit-cell transfer matrix to compute the scattered amplitudes across a finite spacetime crystal. Finally, conclusions are provided in Sec. 7.

2 Preliminaries

2.1 Physical Nature of a Modulated Spacetime Interface

Modulated spacetime interfaces should be understood as perturbations propagating in a stationary medium. This may be understood using the following analogy: consider a chain of standing domino tiles, sufficiently closely spaced to topple their neighbors upon falling so that a chain reaction can be launched by knocking down the first tile. In such a reaction, one clearly sees the "interface" between the fallen and standing parts of the chain propagating along the structure at a specific velocity, with the dominoes themselves on either side of the interface either standing or fallen but not moving in the direction of propagation. The velocity of such an interface along the chain would be limited by the time it takes for one tile to topple the next. We could nevertheless imagine the situation where the tiles could be knocked down by independent external triggers distributed along the domino chain. If these triggers were activated successively at vanishingly small time intervals, the interface velocity would be superluminal, and it would even be infinite if the triggers were operated simultaneously. We stress again that the interfaces described above should be distinguished from the moving interfaces that constitute an altogether different physical system due to the physical movement of the media. For example, in such structures, the superluminal regime is physically prohibited.

2.2 Spacetime Diagrams

Subluminal and superluminal modulation regimes give rise to distinct physics[27,42,43] and require distinct treatments. Figures 2(a) and 2(b) sketch the interaction of an incident wave with a spacetime interface. In the subluminal case of Fig. 2(a), the incident wave catches up with the receding interface. In the superluminal case of Fig. 2(b), the interface, which is faster than the wave, overcomes the incident wave, which was launched earlier. Figures 2(c) and 2(d) graphically summarize the scattering from a subluminal interface and from a superluminal interface in spacetime diagrams, with corresponding spacetime interface trajectories (white and gray areas), wave trajectories (in blue), scattering coefficients (in black), and relevant

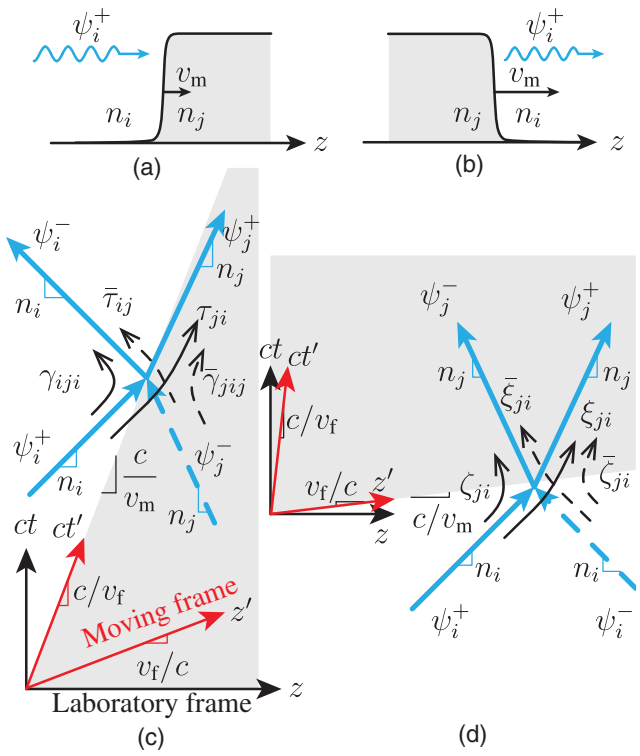

Fig. 2 Scattering at a spacetime interface. The white and gray regions correspond to media i and j, with refractive indices n_i and n_j ($n_i < n_j$). (a) Sketch of a wave incident on a subluminal interface. (b) Same as (a) but for a superluminal interface. (c) Scattering from a subluminal ($v_m < c$) interface in a spacetime diagram. The blue arrows represent wave trajectories (referring to a specific phase point of the waveform), and the black arrows represent scattering coefficients. The dashed lines correspond to incidence from the right. The laboratory and moving frames are superimposed with common origin, and the moving frame has the same velocity as the interface ($v_f/c = v_m/c$). (d) Same as (c) but for a superluminal interface ($v_m > c$), with moving frame having the inverse velocity of the interface ($v_f/c = c/v_m$).

spacetime coordinate frames (laboratory frame in black and moving frame in red).

Given our assumption that the transitions between the homogeneous media i and j forming the crystal are step-like transitions, the spacetime interface problem is mathematically described by the following refractive index function:

$$n(z - v_m t) = n_i + (n_j - n_i)\theta(z - v_m t), \tag{1a}$$

for Fig. 2(a) and

$$n(t - z/v_m) = n_i + (n_j - n_i)\theta(t - z/v_m), \tag{1b}$$

for Fig. 2(b), where $\theta(\cdot)$ is the Heaviside step function and v_m is the velocity of the modulated interface. Although such a step transition cannot be realized in practice, the step profile is an adequate description of it as long as the transition width is smaller that the wavelength in the subluminal case or the transition time is smaller than the period in the superluminal case.

The problem of scattering from gradual spacetime interfaces does not generally admit closed-form solutions, but solutions for specific gradual profile may be found.[45,46] In the case of a crystal, scattering from gradual spacetime profiles are found using a coupled-mode approach.[42,43] Note also that setting $v_m = 0$ in Eq. (1a) reduces the interface to a purely spatial one while setting $v_m = \infty$ in Eq. (1b) reduces the interface to a purely temporal one. Purely spatial and purely temporal problems have been widely investigated, and our results throughout the paper may be verified to correspond to those in the literature at these limit cases. Also note that Eqs. (1a) and (1b) are different from each other, because we have chosen here to have the incident wave always in medium i, for symmetry with respect to the luminal axis $ct = z$; the other option would have been to use Eq. (1a) for all regimes, with an increasing v_m corresponding to a rotation of the interface in Fig. 2(a). In that case, the incidence medium would be different for the subluminal or superluminal regimes. The symmetry between subluminal and superluminal problems will be further discussed in Sec. 2.3.

The trajectories of the interfaces in the spacetime diagrams of Fig. 2 have a slope that is inversely proportional to their velocity, i.e., equal to $\partial(ct)/\partial z_{traj.}(t) = [\partial z_{traj.}(t)/\partial(ct)]^{-1} = c/\text{velocity}$. The slope is therefore steeper for the subluminal case than for the superluminal case. Since the media at either side of the interface are homogeneous, the waves propagate in them at uniform velocities $v_i = c/n_i$ and $v_j = c/n_j$, which correspond to straight trajectories with slopes $c/v_i = n_i$ and $c/v_j = n_j$. Thus, the slopes of the wave trajectories are steeper in the slower, or denser, medium j. Throughout the paper, we restrict our analysis to nondispersive structures, which would be a valid approximation in a system of moderate dispersion. In a regime of stronger dispersion, the velocity of the reflected wave would be different from that of the incident wave given the frequency shift induced by the interface.

The waves in medium (i, j) in the $\pm z$ directions are denoted $\psi^{\pm}_{i,j}$, with ψ representing any of the transverse components of the electromagnetic fields $\mathbf{E}$, $\mathbf{D}$, $\mathbf{H}$, and $\mathbf{B}$.[47] The scattering problem for incidence from the left is called the forward problem, and for incidence from the right, the backward problem. The scattering coefficients for the forward problem are γ and τ for the subluminal regime and ζ and ξ for the superluminal regime, and the scattering coefficients for the backward problem are denoted by barred oversets ($\bar{\gamma}$, $\bar{\tau}$ and $\bar{\zeta}$, $\bar{\xi}$) that we shall simply refer to as "barred" for conciseness. All these coefficients are detailed in Sec. 3.1. Note that the incident wave can propagate in the same direction as the interface or medium, i.e., $\text{sgn}(v_{inc}) = \text{sgn}(v_m)$, as in Fig. 2, or in the direction opposite to the interface or medium, i.e., $\text{sgn}(v_{inc}) = -\text{sgn}(v_m)$. These two cases, which we refer to here as codirectional and contradirectional, respectively, are important to distinguish because they involve drastically different physics, as clearly apparent in the Doppler phenomenon.

To solve scattering problems involving constant velocities, we will use the Lorentz transformations between the laboratory frame and the moving frame, moving at the uniform velocity v_f. These frames are shown in Fig. 2, with coordinates axes (z, ct) and (z', ct'), respectively. In the subluminal case [Fig. 2(a)], the interface appears stationary in the moving frame, i.e., the ct' axis is parallel to the interface. In the superluminal case [Fig. 2(b)], the interface appears purely temporal in the moving frame, i.e., the z' axis is parallel to the interface. The justification for this choice is provided in Sec. 2.6.

2.3 Spacetime Duality

Subluminal and superluminal structures are symmetric around the light line ($z = ct$) in the spacetime diagram, as shown in Fig. 3 for the cases of an interface and a slab. This symmetry is due to the fact that changing from a subluminal to a superluminal problem reverts to exchanging space and time: $v_{\mathrm{sub}}/c = \partial z/\partial(ct) \leftrightarrow \partial(ct)/\partial z = c/v_{\mathrm{sub}} = v_{\mathrm{sup}}/c$. The subluminal and superluminal structures are thus related through a spacetime inversion. This geometrical symmetry manifests a fundamental duality between the subluminal and superluminal problems.

This structural duality is completed by the spacetime duality of Maxwell equations. Consider for instance the electric field in any of the (homogeneous) media on either side of the discontinuities,

$$\frac{\partial^2 E_x}{\partial z^2} - n^2(z - v_{\mathrm{m}}t)\frac{\partial^2 E_x}{\partial (ct)^2} = 0. \tag{2}$$

Interchanging space and time in this equation, and also applying $n \to 1/n$ since $n = c/v = \partial(ct)/\partial z$ and $v_{\mathrm{m}}/c \to c/v_{\mathrm{m}}$ indeed transforms the equation into itself. Thus, the wave equation is also symmetric under spacetime inversion.

Therefore, subluminal and superluminal spacetime electromagnetic problems are the dual of each other. Table 1 lists the variables related to the spacetime duality. The first four row substitutions are the ones just discussed for the problem of an interface. The fifth row refers to the duality between the length ℓ of a subluminal slab and the duration cd of a superluminal slab, as illustrated in Fig. 3(b). The sixth and seventh rows correspond to the duality of plane wave solutions in spacetime scattering problems.

Note that the duality between space and time is incomplete, because one can go backward in space but not in time. As a consequence, we shall see that the scattering coefficients are not related to each other, although the phase quantities will always be. Therefore, once the phase quantities are found for the subluminal case, the phases for the superluminal case are deduced by applying the substitutions noted in Table 1.

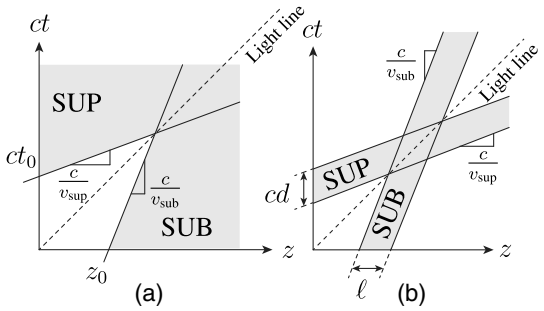

Fig. 3 Spacetime-inversion symmetry of subluminal (SUB) and superluminal (SUP) structures. (a) Interfaces. (b) Slabs.

Table 1 Duality transformations between the subluminal and superluminal regimes.

Subluminal regime		Superluminal regime	
Space	z	Time	ct
Time	ct	Space	z
Modulation velocity	v_{m}/c	Inverse velocity	c/v_{m}
Refractive index	n	Inverse index	$1/n$
Phase velocity	$v/c = 1/n$	Inverse phase velocity	$c/v = n$
Length	ℓ	Duration	cd
Wavelength	λ	Period	cT
Frequency	ω/c	Wavenumber	k

2.4 Interluminal Regime

In the preceding sections, we distinguished the subluminal and the superluminal regimes but omitted to discuss a third velocity regime, which we will describe here. To be more precise, we should refer to a modulated system as strictly subluminal when the modulation is slower than the slowest wave involved, i.e., here, $v_{\mathrm{m}} < v_j$, with $v_j < v_i$, and strictly superluminal when it is faster than the fastest wave involved, i.e., here, $v_{\mathrm{m}} > v_i$. The velocity range between these two regimes, $v_j \leq v_{\mathrm{m}} \leq v_i$, corresponds to a third regime, which we call here the interluminal regime. This regime involves yet different physics and requires yet a different treatment than the strictly sub- and superluminal regimes, as shown in Fig. 4: the incident wave in medium i scatters a single wave in the codirectional case [Fig. 4(a)] and three waves in the contradirectional case [Fig. 4(b)].[48–50]

Let us first consider the codirectional case. In the forward problem of the strictly subluminal regime [Fig. 2(a)], the incident wave, ψ_i^+, is scattered into a reflected wave, ψ_i^-, and a transmitted wave, ψ_j^+. Progressively increasing v_{m}, and therefore decreasing the slope of the interface, brings the interface closer and closer to the trajectory of the transmitted wave. At the point where the interface propagates at the same velocity as the wave transmitted in medium j, i.e., $v_{\mathrm{m}} = v_j$, a shock wave is produced from the accumulation of the transmitted wave at the interface. This is the upper limit of the strictly subluminal regime and the lower limit of the interluminal regime. Beyond this limit ($v_{\mathrm{m}} > v_j$, but still with $v_{\mathrm{m}} < v_i$), the incident wave cannot penetrate any more into medium j because it would otherwise be overtaken by the interface. Thus, scattering reduces here to a single reflected wave. Further increasing the

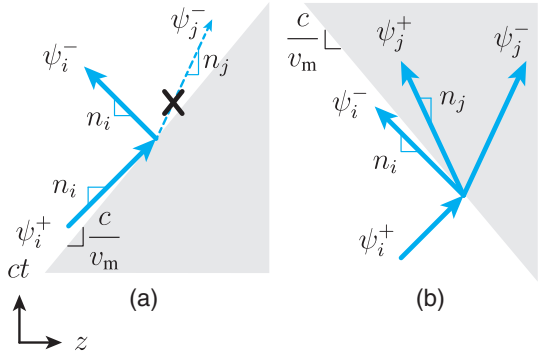

Fig. 4 Graphical description of the interluminal regime in spacetime diagram. (a) Codirectional case, with a single scattered wave. (b) Contradirectional case, with three scattered waves.

velocity leads to the situation where the interface propagates at the same velocity as the incident wave, i.e., $v_m = v_i$. At this point, the incident wave is barely catching up with the interface and so reflection tends to zero. Beyond this limit, we enter the strictly superluminal regime, where the incident wave cannot catch up with the interface unless it was launched earlier than it, which is the case in Fig. 2(b).

For the contradirectional case, we perform a similar thought experiment: starting with a strictly subluminal contradirectional problem, by setting a negative slope for the interface in Fig. 2(a), and increasing the velocity, we arrive to a point where the velocity of the modulation is equal to the velocity of the wave in the media, i.e., $v_m = -v_j$, and so a wave will form, propagating along the interface. The scattering will therefore include three waves: a reflected wave, a later backward wave, and a later forward wave. For a further increased velocity, the interface catches up with the reflected wave, i.e., $v_m = -v_i$, leading to another shock wave from the accumulation of the reflected wave. Beyond this limit, we enter the strictly superluminal regime.

In this paper, we focus on the strictly subluminal and strictly superluminal regimes, which we call subluminal or superluminal for brevity.

2.5 Recall of Special Relativity Concepts

We noted in Sec. 2.2 that we will use Lorentz transformations between the laboratory and moving frames to solve spacetime problems. We present here a brief recall of the Lorentz transformation tools required for this.

2.5.1 Lorentz transformations and Lorentz frames

Intervals of space and time in frames moving at a relative velocity v_f are related through the Lorentz transformations[51]

$$z' = \gamma\left(z - \frac{v_f}{c}ct\right), \quad ct' = \gamma\left(ct - \frac{v_f}{c}z\right), \tag{3}$$

where

$$\gamma = (1 - v_f^2/c^2)^{-1/2} \tag{4}$$

is the Lorentz factor, and where the primed and unprimed quantities refer to quantities measured in the moving frame and in the laboratory frame, respectively. The inverse relations are found by exchanging the primed and unprimed quantities and replacing v_f by $-v_f$ in Eq. (3):

$$z = \gamma\left(z' + \frac{v_f}{c}ct'\right), \quad ct = \gamma\left(ct' + \frac{v_f}{c}z'\right). \tag{5}$$

From these Lorentz transformations, we may superimpose laboratory and moving frames onto the same spacetime plot, as done in Fig. 2. The laboratory frame coordinates are chosen to be orthogonal, and so the moving frame coordinates must be skewed, with the axes slopes found as follows. The z' axis corresponds to $ct' = 0$. Enforcing this in Eq. (5) yields $ct = (v_f/c)z$, which provides v_f/c for the slope of the z' axis. Similarly, the ct' axis corresponds to $z' = 0$, and enforcing this in Eq. (5) yields the $z = (v_f/c)ct$, which provides c/v_f for the ct' axis slope.

2.5.2 Velocity addition formula

Velocities measured in different frames do not simply differ by the frame velocity, i.e., the velocity measured in the laboratory frame, v, is not the sum of the moving frame velocity, v_f, and the velocity measured in the moving frame, $v' = \mathrm{d}z'/\mathrm{d}t'$. The correct relationship between the velocities measured in the different frames is found by applying the chain rule to the definition of v, $v = \mathrm{d}z/\mathrm{d}t$, and replacing the resulting terms by the derivative of the first relation of Eq. (5) with respect to t' and by the derivative of the second relation of Eq. (3) with respect to t, i.e.,

$$v = \frac{\mathrm{d}z}{\mathrm{d}t'}\frac{\mathrm{d}t'}{\mathrm{d}t} = \gamma^2(v' + v_f)\left(1 - \frac{v_f v}{c^2}\right), \tag{6}$$

and solving for v. The result is

$$v = \frac{v' + v_f}{1 + \frac{v'v_f}{c^2}} \tag{7a}$$

and the inverse is

$$v' = \frac{v - v_f}{1 - \frac{vv_f}{c^2}}. \tag{7b}$$

2.5.3 Spectral Lorentz transformations

The phase of a wave is observer-independent.[52] For instance, different observers agree whether a wave is at a maximum or at a minimum, although they do not agree on the distance between two maxima (wavelength) and the time between two maxima (period). Thus

$$\phi^{\pm\prime} = \phi^{\pm}, \tag{8}$$

with the phases defined as

$$\phi^{\pm} = k^{\pm}z \mp \omega^{\pm}t, \quad \phi^{\pm\prime} = k^{\pm\prime}z' \mp \omega^{\pm\prime}t', \tag{9}$$

where the wavenumbers $k^{\pm}$ are related to the corresponding frequencies through the dispersion relation $k^{\pm} = \pm\omega^{\pm}/v$. Using the expressions for z and t in Eq. (5), and resolving in Eq. (8) provides the frequency and wavenumber transformations

$$k^{\pm\prime} = \gamma\left(k^{\pm} \mp \frac{v_f}{c}\frac{\omega^{\pm}}{c}\right), \quad \frac{\omega^{\pm\prime}}{c} = \gamma\left(\frac{\omega^{\pm}}{c} \mp \frac{v_f}{c}k^{\pm}\right). \tag{10}$$

Comparing these transformation with Eq. (3) reveals that k^+ and ω^+/c transform as z and ct.

2.5.4 Field transformations

Consider harmonic plane waves propagating along $\pm z$ with the electric field phasor $\mathbf{E} = E_x\hat{x}$ and magnetic field $\mathbf{H} = H_y\hat{y}$. These fields may be written as

$$E_x^{\pm} = A^{\pm}\mathrm{e}^{\pm i\phi^{\pm}}, \quad \text{with } \phi^{\pm} = k^{\pm}z \mp \omega^{\pm}t. \tag{11}$$

For later use, we relate the other fields to $E_x^{\pm}$ through the wave impedance $\eta = \sqrt{\mu/\epsilon}$ and phase velocity $v = 1/\sqrt{\epsilon\mu}$ as

$$H_y^{\pm} = \mp \frac{1}{\eta} E_x^{\pm}, \tag{12a}$$

$$B_y^{\pm} = \mp \frac{1}{v} E_x^{\pm}, \tag{12b}$$

$$D_x^{\pm} = \epsilon E_x^{\pm} = \frac{1}{v\eta} E_x^{\pm}, \tag{12c}$$

which follow from Maxwell equations, with the assumption of a purely dielectric medium having a purely real and positive permittivity, and no spatial or temporal dispersion.

The fields measured in the laboratory and moving frames are related through[53,54]

$$E_x' = \gamma(E_y - v_\mathrm{f} B_y), \quad H_y' = \gamma(H_x - v_\mathrm{f} D_x), \tag{13a}$$

$$D_x' = \gamma\left(D_x - \frac{v_\mathrm{f}}{c^2} H_y\right), \quad B_y' = \gamma\left(B_y - \frac{v_\mathrm{f}}{c^2} E_x\right), \tag{13b}$$

with the inverse relations again obtained by changing the sign of v_f and interchanging the primed and unprimed quantities. The primed counterpart of Eq. (11) therefore reads

$$E_x^{\pm'} = A^{\pm'} \mathrm{e}^{\pm i\phi^{\pm'}}, \quad \text{with } \phi^{\pm'} = k^{\pm'} z' \mp \omega^{\pm'} t', \tag{14}$$

and the primed counterparts of Eqs. (12) are presented in Appendix A (Sec. 8). For later use, we note that the phase velocity $v^{\pm'}$ transforms as Eqs. (7)[52,55] but with a negative sign for v_f since media appear to be moving in the $-z$ direction if the frame is moving in the $+z$ direction. Thus, the phase velocity in the moving frame is

$$v^{\pm'} = \frac{v^{\pm} + v_\mathrm{f}}{1 + \frac{v^{\pm} v_\mathrm{f}}{c^2}}. \tag{15}$$

2.6 Resolution Strategy

Electromagnetic problems involving moving media are conventionally solved in the moving frame where the system is stationary. The solutions are then converted back to the laboratory frame using Lorentz transformations. The situation for modulated media is more subtle. The overall medium is stationary, with the perturbation propagating through it. In a moving frame having the same velocity as the perturbation, the perturbation appears stationary; however, the media on both sides of it appear to be in motion. As we show in Appendix A (Sec. 8), moving media appear bianisotropic.[52,56,57] The complexity associated with such a bianisotropy defeats the original purpose of using the Lorentz transformation. In order to resolve this complication, we resort to the following hybrid strategy: we first apply the field continuity conditions in the moving frame, then transform the results to the laboratory frame, and finally apply the constitutive relations or the dispersion relations in the laboratory frame.

We stated in Sec. 2.2 that the moving frames for the subluminal and superluminal problems were chosen such that the problems appeared purely spatial or purely temporal, respectively, in the moving frames. We now revisit this statement in the light of the space and time Lorentz transformations presented in Sec. 2.5.1.

In the subluminal regime [Fig. 2(a)], we select the moving frame so that it is copropagating with the interface, at a velocity equal to that of the interface, $v_\mathrm{f} = v_\mathrm{m}$, as conventionally done. The interface is then purely spatial (stationary) in that frame, positioned here at $z' = 0$, which corresponds to the ct' axis being parallel to the interface.

In the superluminal regime [Fig. 2(b)], as discussed in Sec. 2.2, the selection of a comoving frame with ($v_\mathrm{f} = v_\mathrm{m}$) is not possible since Lorentz transformations apply only to frames moving at subluminal velocities. Indeed, the corresponding superluminal Lorentz transformations would result in nonphysical imaginary space and time quantities, as can be seen by setting $v_\mathrm{f} > c$ in Eq. (4). Instead, we choose a frame where the interface appears to be purely temporal (sudden change of material properties at a given time t'), occurring here at $t' = 0$, which corresponds to the z' axis being parallel to the interface.[58] We then graphically find that the moving frame velocity is $c/v_\mathrm{m} = v_\mathrm{f}/c$. We may also find this result mathematically by inspecting Eq. (7b) and finding the condition for $v_\mathrm{m}' = \infty$, which was shown in Sec. 2.2 to correspond to a purely temporal interface (instantaneous change in the material properties). Since $v_\mathrm{m} > c$, we have $v_\mathrm{f} < c$, and the Lorentz transformations are now applicable.

3 Spacetime Interface

3.1 Scattering Coefficients

In this section, we compute the scattering coefficients (denoted by lowercase Greek symbols in Fig. 2) for the case of a single interface that moves with a uniform velocity v_m through the stationary media characterized by two distinct refractive indices n_i and n_j, respectively, to the left and to the right of the interface. We start with the subluminal regime following the strategy outlined in Sec. 2.6. First, we derive the continuity conditions at the interface in the moving frame that has the same velocity as that of the interface, $v_\mathrm{f} = v_\mathrm{m}$, as was suggested in Sec. 2.6. Since the interface appears purely spatial in the moving frame, the usual boundary conditions apply in it, i.e.,

$$E_{xi}' = E_{xj}'|_{z'=0}, \quad H_{yi}' = H_{yj}'|_{z'=0}, \tag{16}$$

which involve the total fields in media i and j, corresponding to $\psi_{i,j} = \psi_{i,j}^{+} + \psi_{i,j}^{-}$ in Fig. 2(a). We next express these fields in terms of their unprimed counterparts using the Lorentz transformations Eq. (13a), which yields the continuity conditions:

$$E_{xi} - v_\mathrm{f} B_{yi} = E_{xj} - v_\mathrm{f} B_{yj}|_{z - v_\mathrm{f} t = 0}, \tag{17a}$$

$$H_{yi} - v_\mathrm{f} D_{xi} = H_{yj} - v_\mathrm{f} D_{xj}|_{z - v_\mathrm{f} t = 0}. \tag{17b}$$

Finally, the frame velocity is set equal to the modulation velocity, i.e., $v_\mathrm{f} = v_\mathrm{m}$.

To study the forward problem, corresponding to incidence $\psi_i^{+} \neq 0$ and $\psi_j^{-} = 0$ (see Fig. 2), we enforce the continuity conditions [Eqs. (17)] by inserting Eq. (11) into Eqs. (17) with $\psi_j^{-} = 0$, which yields

$$\gamma_{iji} = \left.\frac{A_i^-}{A_i^+}\right|_{A_j^-=0} = \frac{\eta_j - \eta_i}{\eta_j + \eta_i}\left(\frac{1 - v_\mathrm{m}/v_i}{1 + v_\mathrm{m}/v_i}\right), \tag{18a}$$

$$\tau_{ji} = \left.\frac{A_j^+}{A_i^+}\right|_{A_j^-=0} = \frac{2\eta_j}{\eta_i + n_j}\left(\frac{1 - v_\mathrm{m}/v_i}{1 - v_\mathrm{m}/v_j}\right). \tag{18b}$$

The subscripts in the reflection coefficient indicate that the wave travels from medium i, reaches medium j, and then reflects back to medium i. This notation will be useful later on, to distinguish forward and backward waves in multiple-interface problems.

The results of Eqs. (18) are valid across the subluminal range, which was shown in Sec. 2.4 to extend from $-v_j$ to v_j. According to Eqs. (18), the transmission coefficient increases monotonically while the reflection coefficients decrease monotonically across this velocity range. In the contradirectional case, the reflection coefficient is greater than in the purely spatial case, whereas in the codirectional case, the reflection is less than in the purely spatial case: the moving interface "cushions" the wave.

We next study the backward problem, corresponding to the incidence $\psi_i^+ = 0$ and $\psi_j^- \neq 0$. Inserting Eq. (11) into Eqs. (17), or alternatively reversing the sign of v_m and exchanging i and j in Eqs. (18), results in

$$\overline{\gamma}_{jij}(v_\mathrm{m}) = \left.\frac{A_j^+}{A_j^-}\right|_{A_i^+=0} = \frac{\eta_i - \eta_j}{\eta_i + \eta_j}\left(\frac{1 + v_\mathrm{m}/v_j}{1 - v_\mathrm{m}/v_j}\right), \tag{19a}$$

$$\overline{\tau}_{ij}(v_\mathrm{m}) = \left.\frac{A_i^-}{A_j^-}\right|_{A_i^+=0} = \frac{2\eta_i}{\eta_j + n_i}\left(\frac{1 + v_\mathrm{m}/v_j}{1 + v_\mathrm{m}/v_i}\right). \tag{19b}$$

We now turn to the superluminal regime. In the moving frame, where the interface appears purely temporal, the continuous fields are[45,59]

$$D'_{xi} = D'_{xj}|_{t'=0}, \quad B'_{yi} = B'_{yj}|_{t'=0}. \tag{20}$$

Applying the Lorentz transformation, Eq. (13b) yields the continuity relations

$$D_{xi} - \frac{v_\mathrm{f}}{c^2}H_{yi} = D_{xj} - \frac{v_\mathrm{f}}{c^2}H_{yj}\bigg|_{t-\frac{v_\mathrm{f}}{c^2}z=0}, \tag{21a}$$

$$B_{yi} - \frac{v_\mathrm{f}}{c^2}E_{xi} = B_{yj} - \frac{v_\mathrm{f}}{c^2}E_{xj}\bigg|_{t-\frac{v_\mathrm{f}}{c^2}z=0}. \tag{21b}$$

We start by studying the forward problem, corresponding to incidence $\psi_i^+ \neq 0$ and $\psi_i^- = 0$. The scattering coefficients are found by inserting Eqs. (12) into Eqs. (21) with $\psi_i^- = 0$, which yields the later backward and later forward coefficients

$$\zeta_{ji} = \left.\frac{A_j^-}{A_i^+}\right|_{A_i^-=0} = \frac{\eta_i - \eta_j}{2\eta_i}\left(\frac{1 - v_\mathrm{m}/v_i}{1 + v_\mathrm{m}/v_j}\right), \tag{22a}$$

$$\xi_{ji} = \left.\frac{A_j^+}{A_i^+}\right|_{A_i^-=0} = \frac{\eta_i + \eta_j}{2\eta_i}\left(\frac{1 - v_\mathrm{m}/v_i}{1 - v_\mathrm{m}/v_j}\right). \tag{22b}$$

The scattering coefficients for the backward problem are found by reversing the velocity sign, but not the exchanging the media, since both waves originate in the same medium, contrarily to the subluminal case, and read

$$\overline{\zeta}_{ji} = \left.\frac{A_j^+}{A_i^-}\right|_{A_i^+=0} = \zeta_{ji}(-v_\mathrm{m}), \tag{23a}$$

$$\overline{\xi}_{ji} = \left.\frac{A_j^-}{A_i^-}\right|_{A_i^+=0} = \xi_{ji}(-v_\mathrm{m}). \tag{23b}$$

Note that Eqs. (17) with the substitution of $v_\mathrm{f} = v_\mathrm{m}$ are identical to Eqs. (21) with the substitution $v_\mathrm{f}/c^2 = 1/v_\mathrm{m}$, which is a consequence of the spacetime duality between subluminal and superluminal regimes, as described in Sec. 2.6. Therefore, the same boundary conditions apply for all regimes. However, we note that the results in the subluminal and the superluminal regime are different: this is due to the fact that in the subluminal case, for the forward problem, $\psi_i^+ + \psi_i^- = \psi_j^+$, whereas for the superluminal case, the reflection is on the other side of the equality sign: $\psi_i^+ = \psi_j^+ + \psi_j^-$. Appendix B (Sec. 9) provides an alternative derivation of the continuity conditions for all regimes.

3.2 Generalization of the Stokes Principle

To facilitate the later study of multiple scattering (Sec. 4), we now establish relations between the scattering coefficients of forward and backward problems derived in Sec. 3.1. This leads to a generalization of the conventional Stokes relations[60] from stationary interfaces to spacetime interfaces.

The conventional Stokes relations are derived upon the basis of a time-reversal symmetry argument: time-reversing, or equivalently, reversing the direction of the waves scattered from an interface returns them to their origin. We extend this argument here to the spacetime interface, with the help of Fig. 5. The subluminal problem is represented in Fig. 5(a). The bottom part of the figure shows the scattering problem that we have already solved, and the top part shows its time-reversed counterpart, where the velocity signs of the two scattered waves have been reversed, along with the velocity sign of the interface. The scattered waves must return to their origin with the same amplitude, from the time-reversal symmetry argument, and the additional scattering possibility must therefore cancel out. Enforcing the symmetry yields then the subluminal generalized Stokes relations, which may be directly read out from the figure as

$$\overline{\gamma}_{iji}\gamma_{iji} + \tau_{ij}\tau_{ji} = 1, \tag{24a}$$

$$\overline{\tau}_{ji}\gamma_{iji} + \gamma_{jij}\tau_{ji} = 0. \tag{24b}$$

From these two generalized Stokes conditions, we find a third relation, which will be used in Sec. 4 to simplify the problem of total scattering from a double interface: barring the unbarred coefficients and unbarring the barred coefficients in Eq. (24a) and

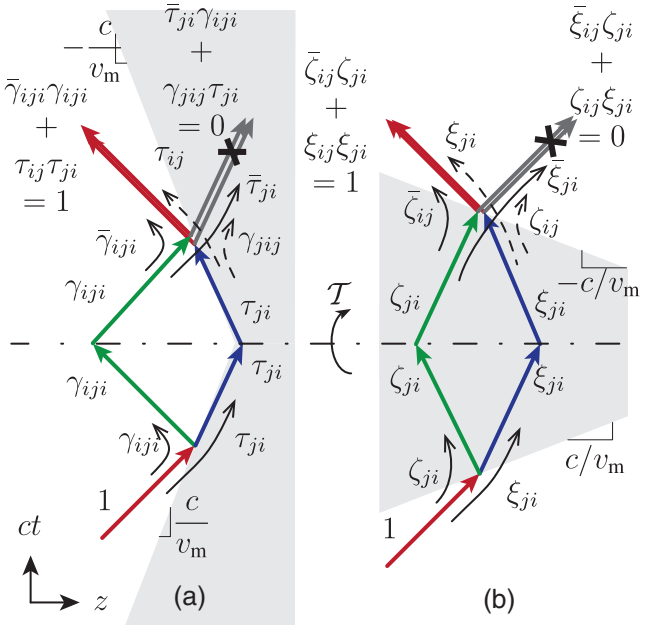

Fig. 5 Generalization of the Stokes principle. (a) Subluminal regime. (b) Superluminal regime.

comparing the resulting equations with the original equation of Eq. (24a), we find that

$$\overline{\tau}_{ij}\overline{\tau}_{ji} = \tau_{ij}\tau_{ji}. \tag{24c}$$

The superluminal case is represented in Fig. 5(b), with the initial problem at the bottom and the time-reversed problem at the top. The generalized superluminal Stokes relations are again read out from the figure, which gives now

$$\overline{\zeta}_{ij}\zeta_{ji} + \xi_{ij}\xi_{ji} = 1, \tag{25a}$$

$$\overline{\xi}_{ij}\zeta_{ji} + \zeta_{ij}\xi_{ji} = 0, \tag{25b}$$

which are of the same form as their subluminal counterparts. An additional relation, which will be used in Sec. 4 to calculate the total scattering from a slab, is found by rewriting Eq. (25b) as $\overline{\xi}_{ij} = -\xi_{ji}\zeta_{ij}/\zeta_{ji}$, exchanging i and j in this relation to obtain $\overline{\xi}_{ji} = -\xi_{ij}\zeta_{ji}/\zeta_{ij}$, and taking the product of these two, to find

$$\overline{\xi}_{ij}\overline{\xi}_{ji} = \xi_{ji}\xi_{ij}. \tag{25c}$$

Barring the unbarred coefficients and unbarring the barred coefficients in Eq. (25a) and using the relation Eq. (25c) leads then to

$$\overline{\zeta}_{ij}\zeta_{ji} = \zeta_{ij}\overline{\zeta}_{ji}. \tag{25d}$$

3.3 Frequency Transitions

The waves scattered from a spacetime interface undergo Doppler-like frequency transitions. We calculate here these frequency transitions, starting again with the subluminal regime. Inserting the moving-frame fields [Eq. (14)] into Eq. (16) leads to the result that the frequencies are conserved in the moving frame, consistently with the fact that the interface is stationary in that frame. We denote this conserved frequency ω_e', with

$$\omega_e' = \omega_i^{+\prime} = \omega_i^{\prime -} = \omega_j^{\prime +}. \tag{26a}$$

Applying the frequency Lorentz transformation [Eq. (10)] to Eq. (26a) with $k_{i,j}^{\pm} = \omega_{i,j}^{\pm}/v_{i,j}$ yields

$$\omega_e = \omega_i^{+}\left(1 - \frac{v_m}{v_i}\right) = \omega_i^{-}\left(1 + \frac{v_m}{v_i}\right) = \omega_j^{+}\left(1 - \frac{v_m}{v_j}\right), \tag{26b}$$

where the relation between ω_e' and ω_e is found by dividing Eq. (26a) by Eq. (26b)

$$\omega_e'/\omega_e = \gamma, \tag{27}$$

with γ being the Lorentz factor given in Eq. (4). The frequency transitions for a backward problem, with the incident wave on the right of the interface, in medium j, would be found by changing the signs of the superscripts, the sign of v_m, and exchanging i and j in Eq. (26b).

Equations (26) are graphically represented in the inverse spacetime diagram of Fig. 6(a). The moving-frame axes k' and ω' are superimposed to the laboratory-frame axes k and ω. The slopes of the moving frame axes, which are v_f/c and c/v_f, from Eq. (10), are written in terms of the interface velocity by setting $v_f = v_m$. The dispersion relations $\omega_{i,j}^{\pm} = k_{i,j}^{\pm}v_{i,j}$ of the two involved media are plotted in the laboratory frame. To find the spectra of the scattered waves, we trace a curve parallel to the k_z' axis with intercept ω_e and locate the spectra of the incident and scattered waves at the intersection of this curve and the dispersion diagrams. Reading out the spectra in the laboratory frame reveals that the reflected wave, ψ_i^-, is downshifted while the transmitted wave, ψ_j^+, is upshifted, consistently with Eq. (26b) for $v_i > v_j$.

For the superluminal regime, we insert the moving-frame fields [Eq. (14)] into Eq. (20) and find the wavenumbers are conserved in the moving frame,

$$k_e' = k_i^{+\prime} = k_j^{\prime +} = k_j^{\prime -}, \tag{28a}$$

where k_e' is the conserved wavenumber.

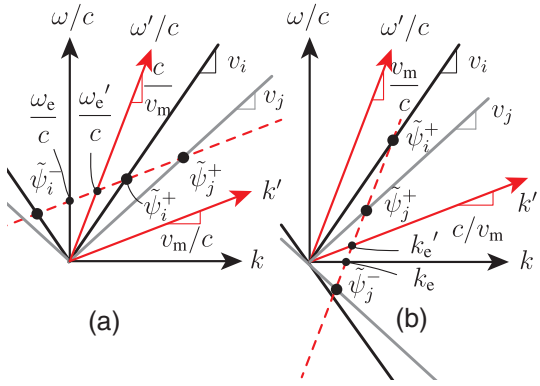

Fig. 6 Frequency transitions at a spacetime interface corresponding to Fig. 2. (a) Subluminal case. (b) Superluminal case.

Applying the wavenumber Lorentz transformation [Eq. (10)] to Eq. (28a) and replacing the frame velocity by the modulation velocity through $v_\mathrm{m} = c^2/v_\mathrm{f}$ with $\omega_{i,j}^{\pm} = k_{i,j}^{\pm} v_{i,j}$ provides

$$k_\mathrm{e} = k_i^+\left(1-\frac{v_i}{v_\mathrm{m}}\right) = k_j^+\left(1-\frac{v_j}{v_\mathrm{m}}\right) = k_j^-\left(1+\frac{v_j}{v_\mathrm{m}}\right). \tag{28b}$$

Dividing Eq. (28a) by Eq. (28b) gives the relation

$$k_\mathrm{e}'/k_\mathrm{e} = \gamma. \tag{29}$$

The frequency transitions for a backward problem, with the incident wave coming from the right, in medium i, would be found by changing the signs of the superscripts and the sign of v_m in Eq. (28b).

Equations (28) are represented graphically in Fig. 6(b). Once again, the axes of the moving frame and the laboratory frame are superimposed. The slopes of the moving frame axes, which are again v_f/c and c/v_f from Eq. (10), are written in terms of the interface velocity, v_m, by setting $v_\mathrm{f}/c = c/v_\mathrm{m}$. The dispersion curves of the two media are drawn, and the conservation of k' is enforced by tracing a line parallel to ω', with intercept k_e. The solutions are located at the intersections of this line and the dispersion diagram of medium j, remembering that both scattered waves are in medium j. Reading out the solutions in the laboratory frame reveals that both waves are downshifted, with ψ_j^- having a negative frequency, associated with time-reversal. As a consequence of time reversal, the wave reflected from a purely temporal interface is refocused to its source[45,61] and the wave reflected from a superluminal interface is refocused to a shifted position.[58]

The results of this section are summarized in Table 2.

4 Spacetime Slab

4.1 Scattering Phenomenology

Noting that the succession of two interfaces corresponds to a slab, we can now address the slab problem upon the basis of Sec. 3. Figure 7 shows the multiple-reflections that occur in sub- and superluminal spacetime slabs. The slabs consist of a medium j sandwiched between media i and k, with media i and k sharing the same parameters. The two interfaces bounding the slab propagate at the same velocity and are thus parallel in the spacetime diagram. The slabs are illuminated by a wave incident from medium i.

The multiple reflections in the subluminal case, represented in Fig. 7(a), and superluminal case, represented in Fig. 7(b), are strikingly different. In the subluminal case, the incident wave is divided into a reflected and a transmitted wave at the first interface. The transmitted wave propagates to the second interface, where it splits into new reflected and transmitted waves, with the former traveling back to the first interface, where it splits again in two parts while the latter reaches the other side of the slab. This process repeats indefinitely, with the amplitudes of the exiting waves decreasing at each round trip. The transmitted wave, ψ_k^+, and the reflected wave, ψ_i^-, are found by summing the infinite contributions.

Table 2 Summary of the scattering formulas, derived in Sec. 3, for a spacetime interface.

Subluminal	Superluminal
Coefficients (Fig. 2)	
$\tau_{ji} = \frac{2\eta_j}{\eta_i+\eta_j}\left(\frac{1-\alpha_i}{1-\alpha_j}\right)$ [Eq. (18b)]	$\xi_{ji} = \frac{\eta_i+\eta_j}{2\eta_i}\left(\frac{1-\alpha_i}{1-\alpha_j}\right)$ [Eq. (22b)]
$\gamma_{iji} = \frac{\eta_j-\eta_i}{\eta_i+\eta_j}\left(\frac{1-\alpha_i}{1+\alpha_i}\right)$ [Eq. (18a)]	$\zeta_{ji} = \frac{\eta_i-\eta_j}{2\eta_i}\left(\frac{1-\alpha_i}{1+\alpha_j}\right)$ [Eq. (22a)]
Frequencies (Fig. 6)	
$\omega_i^- = \omega_i^+\frac{1-\alpha_i}{1+\alpha_i}$ [Eq. (26b)]	$k_j^- = k_i^+\frac{1-1/\alpha_j}{1+1/\alpha_i}$ [Eq. (28b)]
$\omega_j^+ = \omega_i^+\frac{1-\alpha_i}{1-\alpha_j}$ [Eq. (26b)]	$k_j^+ = k_i^+\frac{1-1/\alpha_i}{1-1/\alpha_i}$ [Eq. (28b)]
$\alpha_{i,j} = v_\mathrm{m}/v_{i,j}$	

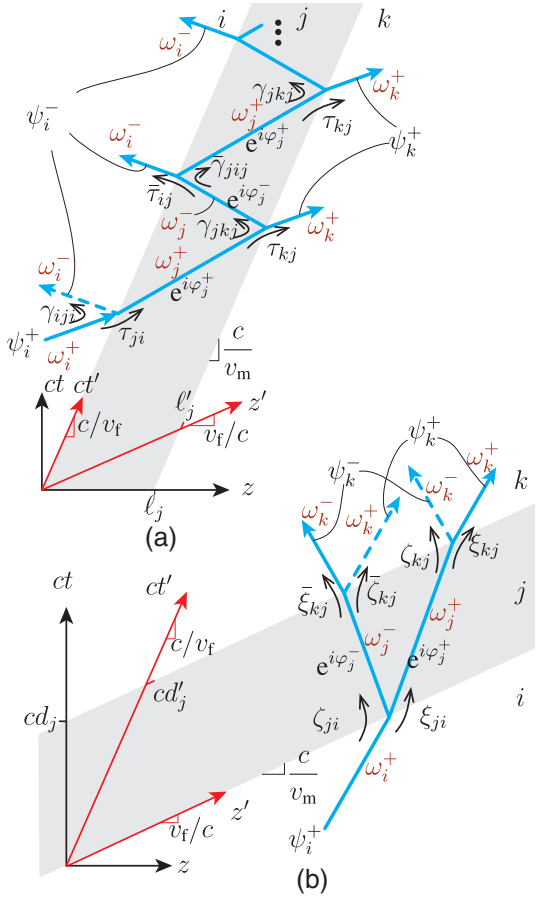

Fig. 7 Multiple-reflection description of the scattering phenomenology in spacetime slabs. Changes in line type (solid ↔ dashed) denote phase reversals. (a) Subluminal slab, with phase change occurring upon reflection to a lower impedance medium ($\eta_j < \eta_i$), according to Eqs. (18). Note that the slope of the trajectories has been altered for representation convenience. (b) Superluminal slab, with phase change occurring upon reflection to a higher impedance medium ($\eta_k > \eta_j$), according to Eqs. (22).

For the superluminal case, represented in Fig. 7(b), the wave incident from medium i splits into a later forward and a later backward wave at the first interface. The two waves propagate then to the second interface, where they split again. However, there is no further scattering so that the total later forward and later backward waves, ψ_k^+ and ψ_k^-, are the sum of only four contributions.

We next calculate the frequency transitions and the phase shifts in the spacetime slabs, to later calculate the amplitudes of the scattered waves.

4.2 Frequency Transitions

Let us start with the subluminal slab. The frequencies, indicated in Fig. 7(a), are calculated by noting, as in Eq. (26a), that the frequencies in the moving frame are conserved, and are all equal to ω_e', i.e.,

$$\omega_e' = \omega_i^{+\prime} = \omega_i^{-\prime} = \omega_j^{+\prime} = \omega_j^{-\prime} = \omega_k^{+\prime}. \tag{30}$$

Applying the frequency Lorentz transformation [Eq. (10)], we obtain the same result as in Eq. (26b) but with the additional frequencies ω_j^- and ω_k^+ scattered from the second interface

$$\begin{aligned}\omega_e &= \omega_i^+\left(1-\frac{v_m}{v_i}\right) = \omega_i^-\left(1+\frac{v_m}{v_i}\right) = \omega_j^+\left(1-\frac{v_m}{v_j}\right)\\ &= \omega_j^-\left(1+\frac{v_m}{v_j}\right) = \omega_k^+\left(1-\frac{v_m}{v_k}\right).\end{aligned} \tag{31}$$

Equation (31) reveals that when media i and k share the same parameters, the wave transmitted through the slab has the same frequency as the incident wave, $\omega_k^+ = \omega_i^+$: it is upshifted to ω_j^+ at the first interface and then downshifted by the same amount at the second interface.

In the superluminal case, the frequencies, indicated in Fig. 7(b), are calculated by noting, as in Eq. (28a), that the wavenumbers in the moving frame are conserved and are all equal to k_e, i.e.,

$$k_e' = k_i^{+\prime} = k_j^{+\prime} = k_j^{-\prime} = k_k^{+\prime} = k_k^{-\prime}. \tag{32}$$

Applying the wavenumber Lorentz transformation [Eq. (10)], these equalities are expressed in the laboratory frame as

$$\begin{aligned}k_e &= k_i^+\left(1-\frac{v_i}{v_m}\right) = k_j^+\left(1-\frac{v_j}{v_m}\right) = k_j^-\left(1+\frac{v_j}{v_m}\right)\\ &= k_k^+\left(1-\frac{v_k}{v_m}\right) = k_k^-\left(1+\frac{v_k}{v_m}\right).\end{aligned} \tag{33}$$

Equation (33) reveals that the later forward wave, ψ_k^+, has the same wavenumber as the incident wave, ψ_i^+, i.e., $k_k^+ = k_i^+$, if media i and k share the same parameters.

4.3 Phase Shift

We start, as usual, with the subluminal case. In the moving frame, where the slab appears stationary, the phase shift of the forward and backward waves is

$$\varphi_j^{\pm\prime} = k_j^{\pm\prime}\ell_j' = \frac{\omega_e'}{v_j^{\pm\prime}}\ell_j', \tag{34}$$

where ℓ_j' is the length of the slab in the moving frame, as shown in Fig. 7(a), and the second equality was found by using the dispersion relation $k_j^{\pm\prime} = \omega_j^{\pm\prime}/v_j^{\pm\prime} = \omega_e'/v_j^{\pm\prime}$, from frequency conservation in the moving frame [Eq. (30)] and with v_j' the phase velocity in the moving frame. We decompose this phase shift as

$$\varphi_j^{\pm\prime} = \bar{\varphi}_j' \pm \Delta\varphi_j', \tag{35a}$$

with the average and difference parts

$$\bar{\varphi}_j' = \frac{\varphi_j^{+\prime} + \varphi_j^{-\prime}}{2} \quad \text{and} \quad \Delta\varphi_j' = \frac{\varphi_j^{+\prime} - \varphi_j^{-\prime}}{2}, \tag{35b}$$

where the bar should not be confused with the bar for the scattering coefficients of the backward problem. Using Eq. (34), these average and difference parts may be written as

$$\bar{\varphi}_j' = \frac{\omega_e'\ell_j'}{2}\left(\frac{1}{v_j^{+\prime}} + \frac{1}{v_j^{-\prime}}\right), \tag{36a}$$

$$\Delta\varphi_j' = \frac{\omega_e'\ell_j'}{2}\left(\frac{1}{v_j^{+\prime}} - \frac{1}{v_j^{-\prime}}\right). \tag{36b}$$

Let us now derive the laboratory-frame counterparts of Eqs. (34) and (36). From phase invariance [Eq. (8)], $\varphi_j = \varphi_j'$, $\bar{\varphi}_j = \bar{\varphi}_j'$, and $\Delta\varphi_j = \Delta\varphi_j'$. The three primed variables ω_e', $v_j^{\pm\prime}$, and ℓ_j' in Eqs. (34) and (36) may be converted to their unprimed counterparts using, respectively, $\omega_e' = \gamma\omega_e$ [Eq. (27)], the equation for $v_j^{\pm\prime}$ in Eq. (15), and the length contraction formula,

$$\ell_j' = \gamma\ell_j, \tag{37}$$

where the lengths ℓ_j and ℓ_j' are indicated in Fig. 7(a) to correspond to the spatial separation between the two parallel lines separating the slab. Equation (37) is obtained by setting $z' = \ell_j'$, $z = \ell_j$, and $ct = 0$ in the left expression of Eq. (3). Applying the three substitutions results in the phase shift counterpart of Eq. (34)

$$\varphi_j^{\pm} = \gamma^2\omega_e\ell_j\frac{1 \mp v_m v_j/c^2}{v_j \mp v_m}, \tag{38a}$$

and the average and difference phase counterparts of Eqs. (36)

$$\bar{\varphi}_j = \omega_e\frac{\ell_j v_j}{v_j^2 - v_m^2}, \tag{38b}$$

$$\Delta\varphi_j = \omega_e\ell_j\gamma^2 v_m\frac{1 - v_j^2/c^2}{v_j^2 - v_m^2}. \tag{38c}$$

For the case of the superluminal slab, the phase shift of the forward and backward waves is found by inserting Eq. (14) into Eq. (20)

$$\varphi_j^{\pm\prime} = \omega_j^{\pm\prime} d_j' = k_e' v_j^{\pm\prime} d_j', \tag{39a}$$

with d_j' as the duration in the moving frame, as drawn in Fig. 7(b). Expressing the phase shift in the form of an average and a difference, as in Eq. (35a), we find

$$\bar{\varphi}_j' = \frac{k_e' d_j'}{2}(v_j^{+\prime} + v_j^{-\prime}), \tag{39b}$$

$$\Delta\varphi_j' = \frac{k_e' d_j'}{2}(v_j^{+\prime} - v_j^{-\prime}). \tag{39c}$$

The superluminal results of Eq. (39) are expressed in terms of laboratory-frame quantities by replacing $k_e' = \gamma k_e$ [Eq. (29)], the equation for $v_j^{\pm\prime}$ in Eq. (15) in which we substitute $v_f = c^2/v_m$, and the duration

$$d_j' = \gamma d_j, \tag{40}$$

where d_j' and d_j are indicated in Fig. 7(b) to correspond to the time separation between the two parallel trajectories delimiting the slab. Equation (40) is obtained by setting $t' = d_j'$, $t = d_j$, and $z = 0$ in the right expression of Eq. (3). Note that Eq. (40) does not correspond to the time dilation equation (which would read $d_j' = \gamma^{-1} d_j$) since time dilation compares the time separation between two fixed events, whereas we are comparing the time separation between two trajectories. Applying the substitutions for k_e', $v_j^{\pm\prime}$ and d_j' into Eqs. (39) yield the phase shift

$$\varphi_j^{\pm} = \gamma^2 k_e d_j \frac{1 \mp c^2/(v_j v_m)}{1/v_j \mp 1/v_m}, \tag{41a}$$

and the average and difference quantities

$$\bar{\varphi}_j = k_e \frac{d_j v_j v_m^2}{v_m^2 - v_j^2}, \tag{41b}$$

$$\Delta\varphi_j = k_e d_j \gamma^2 v_m c^2 \frac{1 - v_j^2/c^2}{v_j^2 - v_m^2}. \tag{41c}$$

Note that Eqs. (41) could have been alternatively found by applying the substitutions of Table 1 into Eqs. (38).

4.4 Scattering Coefficients

For the subluminal case, the reflection coefficient for the forward problem is found by summing up the amplitude of the wave reflected at the first interface, the amplitude of the wave having traveled one round trip, the amplitude of the wave having traveled two round trips and so on, which yields

$$\begin{aligned}\Gamma_{iki} &= \frac{|\psi_i^-|}{|\psi_i^+|} \\ &= \gamma_{iji} + \overline{\tau}_{ij}\gamma_{jkj}\tau_{ji}e^{2i\bar{\varphi}_j} + \overline{\tau}_{ij}\gamma_{jkj}\overline{\gamma}_{jij}\gamma_{jkj}\tau_{ji}e^{4i\bar{\varphi}_j} \\ &\quad + \overline{\tau}_{ij}\gamma_{jkj}(\overline{\gamma}_{jij}\gamma_{jkj})^2\tau_{ji}e^{6i\bar{\varphi}_j} \\ &= \gamma_{iji} + \overline{\tau}_{ij}\gamma_{jkj}\tau_{ji}e^{2i\bar{\varphi}_j}\sum_{n=0}^{\infty}(\overline{\gamma}_{jij}\gamma_{jkj}e^{2i\bar{\varphi}_j})^n,\end{aligned} \tag{42}$$

which is the same expression as that for a stationary slab,[62] but with the local generalized coefficients, Eqs. (18) and (19), and the phases $\bar{\varphi}_j$ in Eq. (38b). Since $\overline{\gamma}_{jij} < 1$ and $\gamma_{jkj} < 1$, the geometric series Eq. (42) reduces to

$$\Gamma_{iki} = \gamma_{iji} + \frac{\overline{\tau}_{ij}\gamma_{jkj}\tau_{ji}e^{2i\bar{\varphi}_j}}{1 - \overline{\gamma}_{jij}\gamma_{jkj}e^{2i\bar{\varphi}_j}} = \gamma_{iji}\frac{1 - e^{2i\bar{\varphi}_j}}{1 - \overline{\gamma}_{jij}\gamma_{jkj}e^{2i\bar{\varphi}_j}}, \tag{43}$$

where the second equality was obtained by using the generalized Stokes condition [Eq. (24)].

The transmission coefficient for the forward problem wave is found by summing the wave traveling through the slab, the wave reflected at the second interface and traveling one round trip, the wave traveling two round trips, and so on, i.e.,

$$\begin{aligned}T_{ki} &= \frac{|\psi_k^+|}{|\psi_i^+|} \\ &= \tau_{kj}\tau_{ji}e^{i\varphi_j^+} + \tau_{kj}\overline{\gamma}_{jij}\gamma_{jkj}\tau_{ji}e^{i\varphi_j^+}e^{2i\bar{\varphi}_j} \\ &\quad + \tau_{kj}(\overline{\gamma}_{jij}\gamma_{jkj})^2\tau_{ji}e^{i\varphi_j^+}e^{2i\bar{\varphi}_j} \\ &= \tau_{kj}\tau_{ji}e^{i\varphi_j^+}\sum_{n=0}^{\infty}(\overline{\gamma}_{jij}\gamma_{jkj}e^{2i\bar{\varphi}_j})^n = \frac{\tau_{kj}\tau_{ji}e^{i\varphi_j^+}}{1 - \overline{\gamma}_{jij}\gamma_{jkj}e^{2i\bar{\varphi}_j}}.\end{aligned} \tag{44}$$

The scattering coefficient extrema are found from Eqs. (43) and (44) to correspond to $\bar{\varphi}_j = n\pi/2$, where n is an integer. For n odd, reflection is maximal and transmission is minimal, and conversely for n even.

The reflection and transmission coefficients for the backward problem are found by barring the unbarred coefficients, unbarring the barred coefficients, and exchanging i and k. The phases $\bar{\varphi}_j$ are unchanged since they correspond to the round trip phase, but the phases φ_j^+ are replaced by φ_j^-. Thus,

$$\overline{\Gamma}_{kik} = \frac{|\psi_k^+|}{|\psi_k^-|} = \overline{\gamma}_{kjk}\frac{1 - e^{2i\bar{\varphi}_j}}{1 - \overline{\gamma}_{jij}\gamma_{jkj}e^{2i\bar{\varphi}_j}} = \Gamma_{iki}\frac{\overline{\gamma}_{kjk}}{\gamma_{iji}}, \tag{45a}$$

$$\overline{T}_{ik} = \frac{|\psi_i^-|}{|\psi_k^-|} = \frac{\overline{\tau}_{ij}\overline{\tau}_{jk}e^{i\varphi_j^-}}{1 - \overline{\gamma}_{jj}\gamma_{jj}e^{2i\bar{\varphi}_j}} = T_{ki}e^{-i\Delta\varphi_j}, \tag{45b}$$

where the third equality in Eq. (45b) was found from a consequence of the Stokes relations [Eq. (24c)]. Note that we are comparing forward and backward problems that have different incident frequencies, ω_i^+ and ω_i^-, respectively, related through ω_e [Eq. (31)] as shown in Fig. 6(a).

In the superluminal case, the situation, although less usual, is simpler since there are now only three scattering events. Reading out Fig. 7(b), we find the later backward and later forward coefficients

$$Z_{ki} = \frac{|\psi_k^-|}{|\psi_i^+|} = \zeta_{kj}\xi_{ji}e^{i\varphi_j^+} + \overline{\xi}_{kj}\zeta_{ji}e^{-i\varphi_j^-}, \tag{46a}$$

$$\Xi_{ki} = \frac{|\psi_k^+|}{|\psi_i^+|} = \xi_{kj}\xi_{ji}e^{i\varphi_j^+} + \overline{\zeta}_{kj}\zeta_{ji}e^{-i\varphi_j^-}. \tag{46b}$$

Applying the generalized Stokes relations for superluminal coefficients [Eqs. (25)], [Eqs. (46)] reduce to

$$Z_{ki} = \zeta_{kj}\xi_{ji}e^{-i\varphi_j^-}(e^{i\bar{\varphi}_j} - 1), \tag{47a}$$

$$\Xi_{ki} = e^{-i\varphi_j^-}[1 + \xi_{kj}\xi_{ji}(e^{i\bar{\varphi}_j} - 1)]. \tag{47b}$$

The scattering coefficient extrema are found from Eqs. (47) to correspond, again, to $\bar{\varphi}_j = n\pi/2$, with n an integer. For n even, both later forward and later backward coefficients are maximal, whereas for n odd, both coefficients are minimal.

The coefficients for the opposite incidence direction, $\overline{Z}_{ki}$ and $\overline{\Xi}_{ki}$, are found by barring and unbarring unbarred and barred coefficients, respectively, and replacing the phase term φ_j^+ by φ_j^-:

$$\overline{Z}_{ki} = \frac{|\psi_k^-|}{|\psi_i^-|} = \overline{\zeta}_{kj}\overline{\xi}_{ji}e^{-i\varphi_j^+}(e^{i\bar{\varphi}_j} - 1) = Z_{ki}\frac{\overline{\zeta}_{kj}\overline{\xi}_{ji}}{\zeta_{kj}\xi_{ji}}e^{i\Delta\varphi_j}, \tag{48a}$$

$$\overline{\Xi}_{ki} = \frac{|\psi_k^+|}{|\psi_i^-|} = e^{-i\varphi_j^+}[1 + \overline{\xi}_{kj}\overline{\xi}_{ji}(e^{i\bar{\varphi}_j} - 1)] = \Xi_{ki}e^{-i\Delta\varphi_j}. \tag{48b}$$

Equations (48) compare the coefficients for the forward and the backward problems having different incident wavenumbers, k_i^+ and k_i^-, respectively, related through k_e in Eq. (33) as represented in Fig. 6(b).

4.5 Interference Condition

The extrema of the scattering coefficients, which were just previously derived, are now analyzed in terms of Bragg-like interference conditions, with the help of Fig. 8.

In the subluminal case, constructive interference occurs in reflection and destructive interference occurs in transmission. The interference condition may be found geometrically by recognizing the triangle with slopes c/v_m and c/v_j has a total length ℓ_j related to the period of the wave T_j^+ through

$$\ell_j = \frac{cT_j^+}{4}\left(\frac{v_m}{c} + \frac{v_j}{c}\right) = \frac{\lambda_j^+}{4}(1 + v_m/v_j), \tag{49}$$

where the second equality is found by using $T_j^+ = \lambda_j^+/v_j$. This can be seen as a generalization of the quarter-wave condition. Inserting Eq. (49) and the definition of ω_e [Eq. (31)] into Eq. (38b) retrieves $\bar{\varphi}_j = \pi/2$.

In the superluminal case, shown in Fig. 8(b), constructive interference occurs for both the later forward and later backward components. The interference condition may be found geometrically by studying the shaded triangle and noticing the total duration cd_j is related to the slopes of the triangle, c/v_m and c/v_j and to the wavelength $\lambda_j^+/4$ through

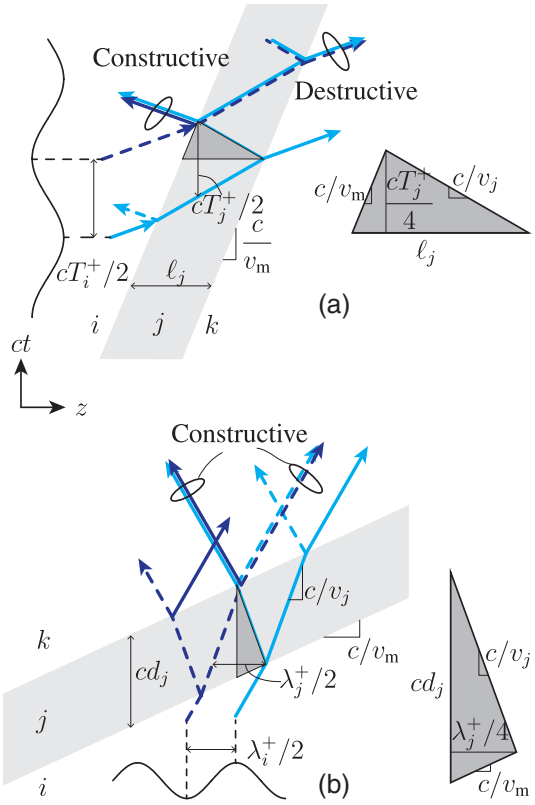

Fig. 8 Graphical Bragg-like interference argument. The light and dark blue trajectories correspond to the maxima and minima of the incident wave, and changes in line type (solid ↔ dashed) denote phase reversals. (a) Subluminal case, with constructive and destructive interference in reflection and transmission, respectively. Note that the slope of the trajectories has been altered for representation convenience. (b) Superluminal case, with constructive interference in both the later forward and later backward waves.

$$cd_j = \frac{\lambda_j^+}{4}\left(\frac{c}{v_j} + \frac{c}{v_m}\right) = \frac{cT_j^+}{4}(1 + v_j/v_m), \tag{50}$$

where $\lambda_j^+ = v_jT_j^+$ was used. Inserting Eq. (50) and the definition of k_e [Eq. (33)] into Eq. (39b) retrieves $\bar{\varphi}_j = \pi/2$.

The spacetime slab results are summarized in Table 3.

5 Unbounded Bilayer Crystal

We now move on to the study of bilayer crystals, whose periodic unit cell is composed of a pair of slabs, or layers, as presented in Fig. 9.

5.1 Linear Approximation of Dispersion Diagram

Crystals are largely described by their dispersion diagrams, which consist in periodic alternances of passbands and stopbands, or bandgaps. The bandgaps are produced by the constructive or destructive interference of the wave scattered by the crystal, as described in Sec. 4.5 for the particular case of a slab. Away from these bandgaps, the waves are transmitted through the crystal without attenuation or amplification, and they undergo little dispersion.

Table 3 Summary of spacetime slab results.

Subluminal regime	Superluminal regime
Phase (Fig. 7)	
$\varphi_j^{\pm\prime} = \bar{\varphi}_j' \pm \Delta\varphi_j'$ [Eq. (35a)]	
$\bar{\varphi}_j = \omega_e \ell_j \dfrac{v_j}{v_j^2 - v_m^2}$ [Eq. (38b)]	$\bar{\varphi}_j = k_e d_j \dfrac{v_j v_m^2}{v_j^2 - v_m^2}$ [Eq. (41b)]
$\Delta\varphi_j = \dfrac{\bar{\varphi}_j \gamma^2 (1 - v_j^2/c^2) v_m}{v_j}$ [Eq. (38c)]	$\Delta\varphi_j = \dfrac{\bar{\varphi}_j \gamma^2 (1 - v_j^2/c^2) c^2}{v_j v_m}$ [Eq. (41c)]
Coefficients (Fig. 7)	
$\Gamma_{iki} = \gamma_{iji} \dfrac{1 - e^{2i\bar{\varphi}_j}}{1 - \bar{\gamma}_{jij}\gamma_{jkj} e^{2i\bar{\varphi}_j}}$ [Eq. (42)]	$Z_{ki} = \zeta_{kj}\xi_{ji} e^{-i\varphi_j^-} (e^{i\bar{\varphi}_j} - 1)$ [Eq. (47)]
$T_{ki} = \dfrac{\tau_{kj}\tau_{ji} e^{i\varphi_j^+}}{1 - \bar{\gamma}_{jij}\gamma_{jkj} e^{2i\bar{\varphi}_j}}$ [Eq. (44)]	$\Xi_{ki} = [1 + \xi_{kj}\xi_{ji}(e^{i\bar{\varphi}_j} - 1)] e^{-i\varphi_j^-}$ [Eq. (47)]
Bragg interference condition (Fig. 8)	
$\ell_j = \dfrac{\lambda_j^+}{4}\left(1 + \dfrac{v_m}{v_j}\right)$ [Eq. (49)]	$d_j = \dfrac{T_j^+}{4}\left(1 + \dfrac{v_j}{v_m}\right)$ [Eq. (50)]

Before presenting the exact construction of the dispersion diagrams, whose complexity occults some of the physics of the problem, we shall derive a simple and useful linear approximation of the exact solution. This approximation consists of a diamond-like grid that coincides with the exact diagram away from the gaps and whose nodes correspond to the exact bandgap centers, as will be shown in Sec. 5.7.

5.1.1 Average velocity

The slopes of the curves in the dispersion diagram of Fig. 10 correspond to the average group velocities, which are inversely proportional to the average refractive indices, $v_{av}^{\pm} = c/n_{av}^{\pm}$. As the approximation is only valid far from the bandgaps, these average refractive indices are only valid in the absence of reflection. The average indices may be found geometrically with the help of Fig. 9 as the slopes of the straight segments connecting the entering and exiting points of the trajectory through the crystal unit cell. This leads to expressions for the average velocities in terms of the refractive indices with weights corresponding to the time spent or distance traveled by the wave in each medium, as shown in Fig. 9.

In the subluminal case, represented in Fig. 9(a), the average index is found as

$$n_{av}^{\pm} = \frac{t_1^{\pm} + t_2^{\pm}}{t_1^{\pm}/n_1 + t_2^{\pm}/n_2}, \tag{51}$$

where the superscript refers to the $\pm z$ wave direction, and where the terms $d_{1,2}^{\pm}$ correspond to the duration of the wave travels in layers 1, 2 in the $\pm$ direction. This average index may be more conveniently written in terms the layer lengths, $\ell_{1,2}$. For this purpose, we express the durations in terms of these lengths, derived in Appendix C (Sec. 10) as

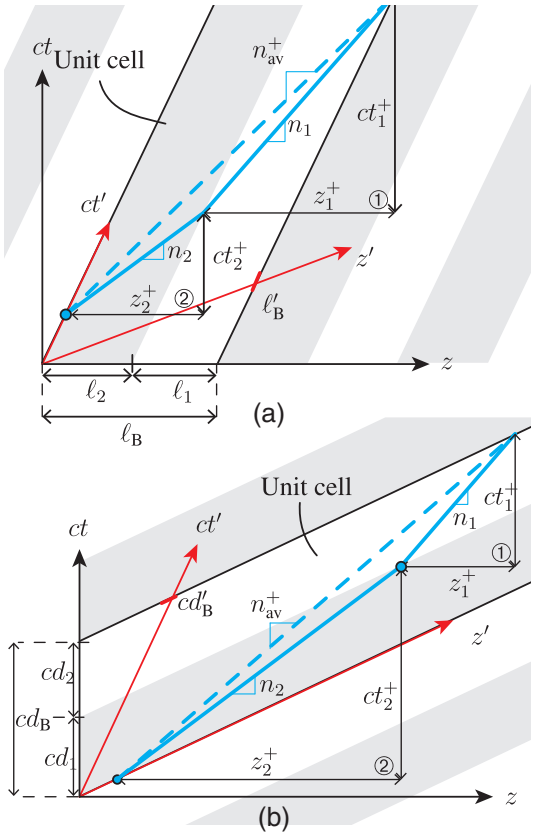

Fig. 9 Bilayer spacetime crystal with spacetime unit cell and out-of-gap wave trajectories. (a) Subluminal equal-length crystal, with $\ell_1 = \ell_2$. The slopes of the triangles ① and ② are $n_1 = ct_1^+/z_1^+$ and $n_2 = ct_2^+/z_2^+$, so $z_1^+ = ct_1^+/n_1$ and $z_2 = ct_2^+/n_2$. Substituting these lengths into the expression for the slope $n_{av} = (ct_1^+ + ct_2^+)/(z_1^+ + z_2^+)$, yields Eq. (51). (b) Superluminal equal-duration crystal, with $d_1 = d_2$. From the slopes of the triangles ① and ②, given in (a), we have $ct_1^+ = z_1^+ n_1$ and $ct_2 = z_2^+ n_2$. Substituting these durations into the expression for the average slope, also given in (a), yields Eq. (55).

$$t_{1,2}^{\pm} = \frac{\ell_{1,2} n_{1,2}/c}{1 \mp v_m n_{1,2}/c}, \tag{52}$$

and insert this relation into Eq. (51), which yields

$$n_{av}^{\pm} = \frac{n_1\ell_1 + n_2\ell_2 \mp v_m n_1 n_2/c(\ell_1 + \ell_2)}{\ell_1 + \ell_2 \mp v_m/c(n_2\ell_1 + n_1\ell_2)}. \tag{53}$$

It is also useful, for later use, to write the expression of the average velocity $v_{av}^{\pm} = c/n_{av}$ in terms of the velocities in the two media, i.e.,

$$v_{av}^{\pm} = \frac{v_1 v_2(\ell_1 + \ell_2) \mp v_m(\ell_1 v_1 + \ell_2 v_2)}{(\ell_1 v_2 + \ell_2 v_1) \mp v_m(\ell_1 + \ell_2)}. \tag{54}$$

In the superluminal case, represented in Fig. 9(b), the average index is found as

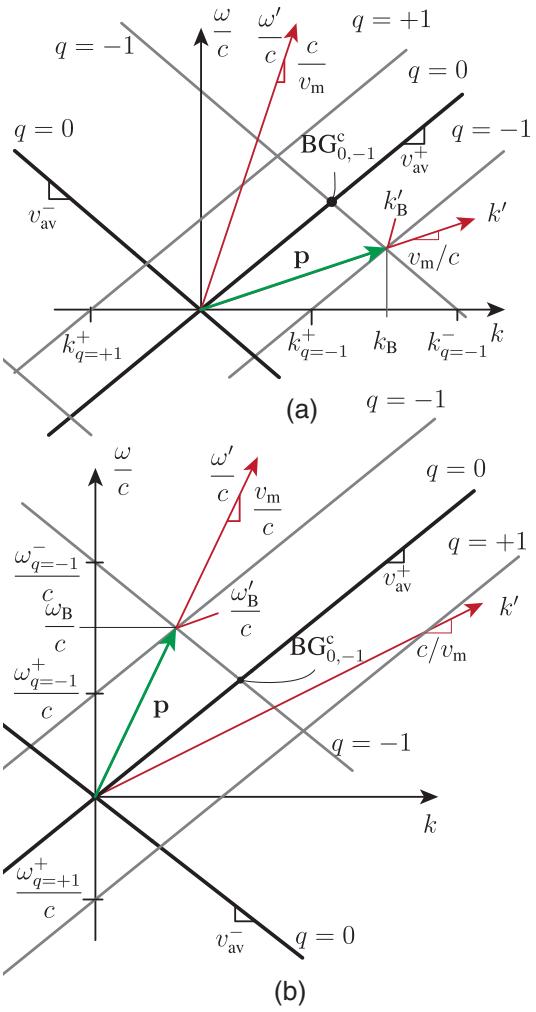

Fig. 10 Linear approximation of the dispersion diagram of bilayer crystals with $n_2/n_1 = 1.5$ and equal electrical lengths. (a) Subluminal case, with $v = (1/3)c$. (b) Superluminal case, with $v = 2c$.

$$n_{\mathrm{av}}^{\pm} = \frac{z_1^{\pm} n_1 + z_2^{\pm} n_2}{z_1^{\pm} + z_2^{\pm}}, \tag{55}$$

where the quantities $z_{1,2}^{\pm}$ correspond to the length traveled by the wave in the $\pm$ direction in layers 1, 2. The average index may be more conveniently written in terms the layer durations $d_{1,2}$. For this purpose, we express the lengths in terms of these durations, derived in Appendix C (Sec. 10), as

$$z_{1,2}^{\pm} = \frac{c d_{1,2}}{n_{1,2} \mp c/v_{\mathrm{m}}}, \tag{56}$$

and insert this relation into Eq. (55), which yields

$$n_{\mathrm{av}}^{\pm} = \frac{d_1 + d_2 \mp c/v_{\mathrm{m}}(d_1/n_2 + d_2/n_1)}{d_1/n_1 + d_2/n_2 \mp c/(v_{\mathrm{m}} n_1 n_2)(d_1 + d_2)}. \tag{57}$$

It is also useful, for later use, to write the expression of the average velocity in terms of the velocities in the two media, i.e.,

Table 4 Average refractive index for different modulation velocities, from (53), with $\ell_1 = \ell_2$ (upper half) and Eq. (57), with $d_1 = d_2$ (lower half).

Modulation regime	Velocity (v_{m})	Average index (n_{av}^{+})	Average index (n_{av}^{-})
Spatial	0	$\frac{1}{2}(n_1 + n_2)$	$\frac{1}{2}(n_1 + n_2)$
Subluminal upper limit	$v_2 = \frac{c}{n_2}$	n_2	$n_2 \frac{3n_1 + n_2}{n_1 + 3n_2}$
Superluminal lower limit	$v_1 = \frac{c}{n_1}$	n_1	$n_1 \frac{3n_2 + n_1}{n_2 + 3n_1}$
Temporal	∞	$\frac{1}{2}\left(\frac{1}{n_1} + \frac{1}{n_2}\right)^{-1}$	$\frac{1}{2}\left(\frac{1}{n_1} + \frac{1}{n_2}\right)^{-1}$

$$v_{\mathrm{av}}^{\pm} = \frac{v_{\mathrm{m}}(d_1 v_1 + d_2 v_2) \mp v_1 v_2 (d_1 + d_2)}{v_{\mathrm{m}}(d_1 + d_2) \mp (d_1 v_2 + d_2 v_1)}. \tag{58}$$

Note that Eqs. (57) and (58) could have been alternatively found by applying the substitutions of Table 1 to Eqs. (53) and (54).

Table 4 lists the forward and backward average refractive indices at special velocity points for unit cells of equal layer length or equal layer duration. The first row gives the average indices for the purely spatial regime, found by setting $v_{\mathrm{m}} = 0$ in Eq. (53). These indices are found to be the same for forward or backward waves and are the arithmetic average of the two indices.

The second row provides the average indices for the upper limit of the subluminal regime (or lower limit of the interluminal regime, see Sec. 2.4) and are found by setting $v_{\mathrm{m}} = c/n_2$ in Eq. (53). The forward average index reduces to n_2 since the wave has the same velocity as the modulation and, therefore, never exits the layer of refractive index n_2. The backward wave travels across both media so that the average index is a function of the two refractive indices.

The third row corresponds to the superluminal lower limit (or upper limit of the interluminal regime, see Sec. 2.4) and is found by setting $v_{\mathrm{m}} = c/n_1$ in Eq. (57). Now, the forward average index reduces to n_1 since the wave remains in medium n_1 while the backward index is the same function as in the previous case with exchanged indices.

The fourth row provides the indices for the purely temporal limit, found by setting $v_{\mathrm{m}} = \infty$ in Eq. (57). The average indices for forward and backward waves are again equal, as is expected since the structure is symmetric in space. Now the inverse of the average index is the arithmetic average of the inverses of two indices, reminiscent of a parallel circuit form. The series and parallel circuit forms of the spatial and temporal average indices are akin to the polarization-dependent form of the average indices in hyperbolic media.[63]

5.1.2 Dispersion diagram period

The first pair of dispersion curves in Fig. 10 (solid lines), $\omega = \pm v_{\mathrm{av}}^{\pm} k$, has its intercept at the origin, whereas the other pairs of curves are (obliquely) translated from this first pair by

$q\mathbf{p} = q(k_\mathrm{B}, \omega_\mathrm{B})$, where q is the integer representing the pair of curves, $\mathbf{p}$ is the spacetime period, and k_B and ω_B are the wavenumber and frequency translation quantities.

In the subluminal case, the spacetime period vector is found by recalling that the crystal is stationary in the moving frame so that the period is simply

$$\mathbf{p}' = (k'_\mathrm{B}, 0) = \left(\frac{2\pi}{\ell'_\mathrm{B}}, 0\right). \tag{59}$$

This period is expressed in terms of laboratory-frame quantities by first applying the wavenumber Lorentz transformations $k'_\mathrm{B} = k_\mathrm{B}/\gamma$ and $k'_\mathrm{B} = \omega_\mathrm{B}/(v_\mathrm{m}\gamma)$, which are found by setting $k' = k'_\mathrm{B}$, $\omega' = 0$, $k = k_\mathrm{B}$, and $\omega = \omega_\mathrm{B}$ in Eq. (10) with $v_\mathrm{f} = v_\mathrm{m}$ (Sec. 2.6), and next applying the length contraction $\ell'_\mathrm{B} = \gamma\ell_\mathrm{B}$ [as in Eq. (37), replacing ℓ_j, ℓ'_j by ℓ_B, ℓ'_B], so that

$$k_\mathrm{B} = \frac{2\pi}{\ell_\mathrm{B}}, \quad \omega_\mathrm{B} = \frac{2\pi v_\mathrm{m}}{\ell_\mathrm{B}}, \tag{60}$$

which may be alternatively obtained from Bloch–Floquet theory.

In the superluminal case, the spacetime period vector is

$$\mathbf{p}' = (0, \omega'_\mathrm{B}) = \left(0, \frac{2\pi}{d'_\mathrm{B}}\right). \tag{61}$$

As for the subluminal case, we express this period into laboratory frame quantities by first applying the frequency transformations $\omega'_\mathrm{B} = \omega_\mathrm{B}/\gamma$ and $\omega'_\mathrm{B} = k_\mathrm{B}/(\gamma v_\mathrm{f}/c^2) = k_\mathrm{B} v_\mathrm{m}/\gamma$, which are found by setting $\omega' = \omega'_\mathrm{B}$, $k' = 0$, $k = k_\mathrm{B}$, and $\omega = \omega_\mathrm{B}$ in Eq. (10) with $v_\mathrm{f} = c^2/v_\mathrm{m}$ (Sec. 2.6). We then apply the time contraction $d'_\mathrm{B} = d_\mathrm{B}/\gamma$, as in Eq. (40), replacing d_j, d'_j by d_B, d'_B, and this gives

$$\omega_\mathrm{B} = \frac{2\pi}{d_\mathrm{B}}, \quad k_\mathrm{B} = \frac{2\pi}{v_\mathrm{m} d_\mathrm{B}}. \tag{62}$$

For both the subluminal and the superluminal cases, we may write the equations for the pairs of curves forming the linear approximation grid as

$$\omega + q\omega_\mathrm{B} = \pm v^\pm_\mathrm{av}(k + qk_\mathrm{B}), \tag{63}$$

so that Fig. 10 may be simply plotted from $v^\pm_\mathrm{av}$ derived in Sec. 5.1 along with the just derived translation quantities.

5.2 Bandgap Center Position

The bandgap centers are located at the nodes of the linear approximation grid we have just derived. The bandgap center $\mathrm{BG}^\mathrm{c}_{0,-1}$ is indicated in Fig. 10 at the intersection of curves $q = 0$ and $q = -1$, where the superscript c refers to the center of the bandgap.

Let us start with the subluminal case. We first derive the k-intercepts of the curves $\omega = v^\pm_\mathrm{av}(k - k^\pm_q)$, with $k^\pm_q$ being the k-intercepts of the forward-wave and backward-wave solutions, found by setting $\omega = 0$ in Eq. (63) as

$$k^\pm_q = \frac{q\omega_\mathrm{B}}{\pm v^\pm_\mathrm{av}} - qk_\mathrm{B} = qk_\mathrm{B}\left(\frac{v_\mathrm{m}}{\pm v^\pm_\mathrm{av}} - 1\right), \tag{64}$$

where the second equation in Eq. (64) was found using Eq. (60)

The position of bandgap $\mathrm{BG}_{0,-1}$ is then found by intersecting the curves representing the two relevant modes, i.e., setting $\omega = v^+_\mathrm{av}k = -v^-_\mathrm{av}(k - k^-_{q=-1})$. Inserting Eq. (64) into this intersection condition results in the bandgap center position

$$k^\mathrm{c}_{0,-1} = \frac{v_\mathrm{m} + v^-_\mathrm{av}}{v^+_\mathrm{av} + v^-_\mathrm{av}} k_\mathrm{B}. \tag{65}$$

The other bandgap centers are found by a similar procedure. This relation reduces to the coupled-mode result[64,65] under the approximation $v^+_\mathrm{av} = v^-_\mathrm{av}$.

For the superluminal regime, we first calculate the ω-intercepts of the forward and backward curve of each mode. These intercepts are found by setting $k = 0$ in Eq. (63), which yields

$$\omega^\pm_q = \pm qk_\mathrm{B} v^\pm_\mathrm{av} - q\omega_\mathrm{B} = q\omega_\mathrm{B}\left(\frac{\pm v^+_\mathrm{av}}{v_\mathrm{m}} - 1\right), \tag{66}$$

with the second equality again obtained using Eq. (62). From these intercepts, we find the intersection position of the bandgap $\mathrm{BG}_{0,-1}$ by intersecting the two curves as $k = \omega/v^+_\mathrm{av} = -(\omega - \omega^\mathrm{b}_{q=-1})/v^-_\mathrm{av}$, which yields

$$\omega^\mathrm{c}_{0,-1} = \frac{v^+_\mathrm{av}}{v_\mathrm{m}} \frac{v^-_\mathrm{av} + v_\mathrm{m}}{v^-_\mathrm{av} + v^+_\mathrm{av}} \omega_\mathrm{B}, \tag{67}$$

which reduce to the coupled-mode results[66] under the approximation $v^+_\mathrm{av} = v^-_\mathrm{av}$. The other bandgap centers are again found by a similar procedure.

5.3 Unit-Cell Transfer Matrix

We now calculate the transfer matrix of a unit cell, extending the classical transfer matrix of stationary structures,[67] with the help of Fig. 11. Note that this graph corresponds, for later illustration convenience, to the particular design of an equal-phase crystal, where the forward and backward round-trip trajectories emerge at the same spacetime point. By definition, the transfer matrix relates the fields in media i and k at the interfaces $I_{i,j}$ and $I_{k,l}$ as

$$\begin{bmatrix} \psi^+_k \\ \psi^-_k \end{bmatrix}_{I_{k,l}} = [M_\mathrm{B}] \begin{bmatrix} \psi^+_i \\ \psi^-_i \end{bmatrix}_{I_{i,j}}, \tag{68}$$

where the two interfaces separate layers i, j and k, l, respectively, as shown in Fig. 11.

The unit-cell matrix is found by multiplying interface matrices, $[T_{ji}]$, and propagation matrices, $[P_j]$, according to Fig. 11, i.e.,

$$[M_\mathrm{B}] = [P_k][T_{kj}][P_j][T_{ji}]. \tag{69}$$

We first calculate the interface matrix, $[T_{m,m-1}]$, which relates the fields at both sides of the interface $I_{m,m-1}$. At the first interface of the unit cell, we have

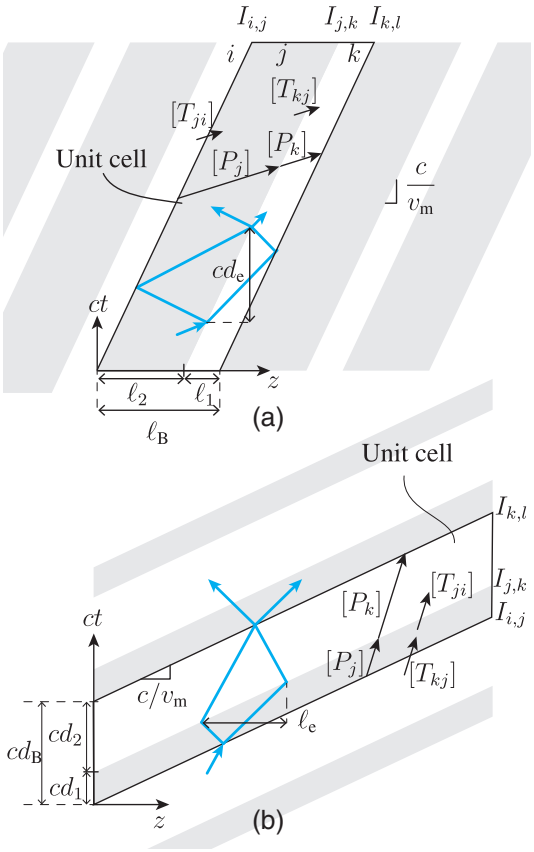

Fig. 11 Bilayer spacetime crystal with spacetime unit cell. (a) Subluminal regime. (b) Superluminal regime.

$$\begin{bmatrix}\psi_j^+\\ \psi_j^-\end{bmatrix}_{I_{i,j}} = [T_{ji}]\begin{bmatrix}\psi_i^+\\ \psi_i^-\end{bmatrix}_{I_{i,j}}. \tag{70}$$

The interface matrix may be computed using the results of Sec. 3 for interface scattering.

In the subluminal case, reading out Fig. 2(a), we write the scattered fields in terms of the incident fields

$$\psi_j^+ = \tau_{ji}\psi_i^+ + \overline{\gamma}_{jij}\psi_j^-, \tag{71a}$$

$$\psi_i^- = \gamma_{iji}\psi_i^+ + \overline{\tau}_{ij}\psi_j^-, \tag{71b}$$

and rearrange these equations to cast them into the form of Eq. (70), i.e.,

$$[T_{ji}^{\mathrm{Sb}}] = \frac{1}{\overline{\tau}_{ij}}\begin{bmatrix}\tau_{ji}\overline{\tau}_{ij} - \overline{\gamma}_{jij}\gamma_{iji} & \overline{\gamma}_{jij}\\ -\gamma_{iji} & 1\end{bmatrix}, \tag{72}$$

where the superscript Sb stands for subluminal. Substituting the interface scattering coefficients [Eqs. (18)] into Eq. (72) yields

$$[T_{ji}^{\mathrm{Sb}}] = \frac{1}{2\eta_i}\begin{bmatrix}(\eta_i+\eta_j)\frac{1-v_m/v_i}{1-v_m/v_j} & (\eta_i-\eta_j)\frac{1+v_m/v_i}{1-v_m/v_j}\\ (\eta_i-\eta_j)\frac{1-v_m/v_i}{1+v_m/v_j} & (\eta_i+\eta_j)\frac{1+v_m/v_i}{1+v_m/v_j}\end{bmatrix}. \tag{73}$$

In the superluminal case, reading out Fig. 2(b), we write the scattered fields in terms of the incident fields as

$$\psi_j^+ = \xi_{ji}\psi_i^+ + \overline{\zeta}_{ji}\psi_i^-, \tag{74a}$$

$$\psi_j^- = \zeta_{ji}\psi_i^+ + \overline{\xi}_{ji}\psi_i^-. \tag{74b}$$

These equations can then be cast into the matrix form of Eq. (70),

$$[T_{ji}^{\mathrm{Sp}}] = \begin{bmatrix}\xi_{ji} & \overline{\zeta}_{ji}\\ \zeta_{ji} & \overline{\xi}_{ji}\end{bmatrix}, \tag{75}$$

with the superscript Sp standing for superluminal. We note that Eq. (75) is much simpler than Eq. (72) since in the superluminal case both incident waves are in the first medium and both scattered waves are in the later medium. In other words, the scattering matrix is equal to the interface matrix for the superluminal case. Although Eqs. (75) and (72) have a very different appearance, inserting Eqs. (22) into Eq. (75) reveals that they are in fact exactly identical, i.e., $[T_{ji}^{\mathrm{Sb}}] = [T_{ji}^{\mathrm{Sp}}]$, consistent with the results of Ref. 44.

We next derive the propagation matrix, which relates the fields at the first and second interface delimiting a given layer. For instance, the propagation matrix of layer j is given as

$$\begin{bmatrix}\psi_j^+\\ \psi_j^-\end{bmatrix}_{I_{j,k}} = [P_j]\begin{bmatrix}\psi_j^+\\ \psi_j^-\end{bmatrix}_{I_{i,j}}. \tag{76}$$

Since there is no scattering and only a phase shift between the interfaces, the matrix simply reads

$$[P_j] = \begin{bmatrix}e^{i\varphi_j^+} & 0\\ 0 & e^{-i\varphi_j^-}\end{bmatrix} = e^{i\Delta\varphi_j}\begin{bmatrix}e^{i\bar{\varphi}_j} & 0\\ 0 & e^{-i\bar{\varphi}_j}\end{bmatrix}, \tag{77}$$

with the phase terms defined in Sec. 4.3. Inserting the interface matrix [Eq. (73)] and the propagation matrix [Eq. (77)] into Eq. (68) yields the unit-cell transfer matrix

$$[M_B] = e^{i\Delta\varphi}\begin{bmatrix}a & ib\\ ic & a^*\end{bmatrix} = e^{i\Delta\varphi}[M_{B0}], \tag{78}$$

where

$$a = e^{i\bar{\varphi}_k}\left[\cos\bar{\varphi}_j + \frac{i}{2}\left(\frac{\eta_j}{\eta_k}+\frac{\eta_k}{\eta_j}\right)\sin\bar{\varphi}_j\right], \tag{79a}$$

$$b = -e^{-i\bar{\varphi}_k}\frac{1}{2}\left(\frac{\eta_j}{\eta_k}-\frac{\eta_k}{\eta_j}\right)\frac{1+v_m/v_j}{1-v_m/v_j}\sin\bar{\varphi}_j, \tag{79b}$$

$$c = e^{i\bar{\varphi}_k}\frac{1}{2}\left(\frac{\eta_j}{\eta_k}-\frac{\eta_k}{\eta_j}\right)\frac{1-v_m/v_j}{1+v_m/v_k}\sin\bar{\varphi}_j. \tag{79c}$$

Equations (79) are valid for both the subluminal regime and the superluminal regime, with the phase expressions $\bar{\varphi}_{j,k}$ and $\Delta\varphi_{j,k}$ provided in Table 3. Matrix $[M_{B0}]$ is unimodular, and so the determinant of M_B in Eq. (78) is $\det[M_B] = e^{i\Delta\varphi}$. Note that this matrix satisfies the conditions $be^{i\Delta\phi} = -b^*$ and $ce^{i\Delta\phi} = -c^*$,[68] which stems from spacetime reversal symmetry, as shown in Appendix D (Sec. 11). Identical results were found by

Biancalana et al. in Ref. 44 using an alternative approach based on a symmetric form of Maxwell equations.

5.4 Dispersion Relation Derivation

The exact dispersion diagram may now be computed using the unit-cell transfer matrix Eq. (78), which we have just derived. From Bloch–Floquet theory, the fields before and after the unit-cell of a crystal are related through $\psi_k^{\pm} = e^{i\Phi_B}\psi_i^{\pm}$, where Φ_B is the Bloch–Floquet phase. This leads to the eignenvalue problem

$$\begin{bmatrix} \psi_k^+ \\ \psi_k^- \end{bmatrix}_{I_{k,l}} = [M_B] \begin{bmatrix} \psi_i^+ \\ \psi_i^- \end{bmatrix}_{I_{i,j}} = e^{i\Phi_B} \begin{bmatrix} \psi_i^+ \\ \psi_i^- \end{bmatrix}_{I_{i,j}}. \tag{80}$$

The eigensolution to this problem is found by substituting Eq. (78) into Eq. (80), grouping the difference phase $e^{i\Delta\varphi}$ with the Bloch–Floquet phase $e^{i\Phi_B}$ so that $([M_{B0}] - e^{i(\Phi_B - \Delta\varphi)}[I])[\psi_i] = 0$, and setting the determinant to zero, i.e.,

$$\begin{vmatrix} a - e^{i(\Phi_B - \Delta\varphi)} & b \\ c & a^* - e^{i(\Phi_B - \Delta\varphi)} \end{vmatrix} = 0. \tag{81}$$

This corresponds to a quadratic equation whose solutions are

$$e^{i(\Phi_B - \Delta\varphi)} = \frac{a + a^*}{2} \pm \sqrt{\left(\frac{a + a^*}{2}\right)^2 - 1}, \tag{82}$$

where the identity $aa^* - bc = 1$ associated with the unimodularity of $[M_{B0}]$ has been applied. Equation (82) may be rewritten in a more standard, trigonometric form by applying the Euler identity $e^{i(\Phi_B + \Delta\varphi)} = \cos(\Phi_B + \Delta\varphi) + i\sin(\Phi_B + \Delta\varphi)$ to the left-hand side of Eq. (82) and writing $i\sin(\Phi_B + \Delta\varphi) = \pm\sqrt{\cos^2(\Phi_B + \Delta\varphi) - 1}$. Comparing the result with the right-hand side of Eq. (82) implies

$$\begin{aligned} \cos(\Phi_B - \Delta\varphi) &= \frac{a + a^*}{2} \\ &= \cos\bar{\varphi}_j \cos\bar{\varphi}_k - \frac{1}{2}\left(\frac{\eta_j}{\eta_k} + \frac{\eta_k}{\eta_j}\right)\sin\bar{\varphi}_j \sin\bar{\varphi}_k, \end{aligned} \tag{83}$$

where Eq. (79) has been used in the second equality.

Equation (83) is the dispersion relation, whose graphical representation corresponds to the dispersion diagram, which we will construct next. We may already note that the phase Φ_B in Eq. (83) may be either real or complex since the right-hand side may be less than 1, and the inverse cosine of a quantity less than one is complex. A real Φ_B phase will be associated with pure propagation, whereas an imaginary Φ_B phase will be associated with either attenuation or amplification, corresponding to bandgaps in the dispersion diagram.

5.5 Construction of Dispersion Diagram

The dispersion relation Eq. (83) essentially relates the Bloch–Floquet phase (Φ_B) and the phases in the layers of the crystal ($\bar{\varphi}$ and $\Delta\varphi$). To plot the dispersion diagram, we must transform this relation into one that relates the frequencies and wavenumbers (ω and k). This may be conveniently done using a set of parametric equations.

We start with the subluminal case. First, we write the Bloch–Floquet phase in terms of the frequency and wavenumber, i.e.,

$$\Phi_B = \Phi_B' = k'\ell_B' = \gamma^2\left(k - \frac{v_m}{c^2}\omega\right)\ell_B, \tag{84}$$

where the last equation used the Lorentz wavenumber transformation Eq. (10) and length contraction Eq. (37). The frequency and wavenumber in Eq. (84) are related to the conserved frequency parameter ω_e through

$$\omega_e = \omega - v_m k, \tag{85}$$

from the fact that $\omega_e' = \omega'$, similarly to Eq. (26). Combining Eqs. (84) and (85) and factoring out ω and k finally yields the parametric equations

$$\omega(\omega_e) = \frac{v_m\Phi_B(\omega_e)}{\ell_B} + \gamma^2\omega_e, \tag{86a}$$

$$k(\omega_e) = \frac{\Phi_B(\omega_e)}{\ell_B} + \gamma^2\frac{v_m^2}{c^2}\omega_e. \tag{86b}$$

To plot the dispersion relations, we first calculate the Bloch–Floquet phase $\Phi_B(\omega_e)$ using Eq. (83), with $\bar{\varphi}_{i,j}(\omega_e)$ and $\Delta\varphi_{i,j}(\omega_e)$ given in Table 3. We then compute $\omega(\omega_e)$ and $k(\omega_e)$ in Eq. (86) independently, for a range of frequencies ω_e, and plot them to obtain the dispersion diagram of Fig. 12(a).

In the superluminal case, the Bloch–Floquet phase is

$$\Phi_B = \Phi_B' = \omega' d_B' = \gamma^2\left(\omega - \frac{c^2}{v_m}k\right)d_B, \tag{87}$$

where the second equality was again found from the Lorentz frequency transformation Eq. (10) and the time contraction Eq. (40). The frequency and wavenumber in Eq. (87) are related to the conserved spatial frequency k_e through

$$k_e = k - \omega/v_m, \tag{88}$$

from the fact that $k_e' = k'$ as in Eq. (28). Combining Eq. (87) with Eq. (88) leads to the parametric equations

$$\omega(k_e) = \frac{\Phi_B(k_e)}{d_B} + \gamma^2\frac{c^2}{v_m}k_e, \tag{89a}$$

and

$$k(k_e) = \frac{\Phi_B(k_e)}{v_m d_B} + \gamma^2 k_e. \tag{89b}$$

The dispersion diagram corresponding to the parametric equations [Eqs. (89)] is plotted in Fig. 12(b) following the same procedure as for the subluminal case, i.e., calculating $\Phi_B(k_e)$ from Eq. (83), with $\bar{\varphi}(k_e)$ and $\Delta\varphi(k_e)$ given in Table 3, and then computing the parametric equations [Eqs. (89)] for $\omega(k_e)$ and $k(k_e)$.

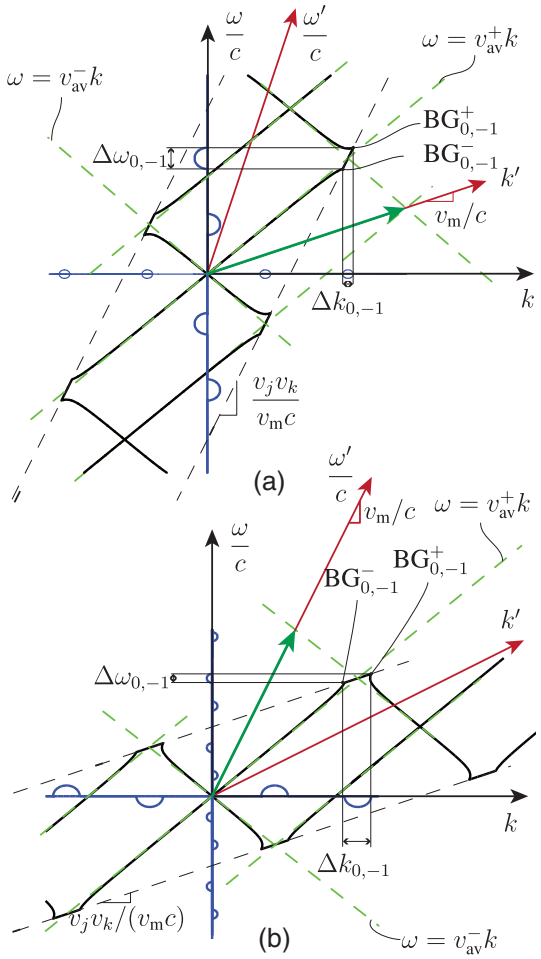

Fig. 12 Dispersion diagram of bilayer crystals with $n_2/n_1 = 1.5$ and equal phases ($\bar{\varphi}_j = \bar{\varphi}_k$). The solid curves correspond to the exact solution [Eqs. (86) and (89)], with the black and blue parts, respectively, corresponding to the real and imaginary parts, and the dashed curves to the linear approximation [Eq. (63)]. (a) Subluminal case, with $v = (1/3)c$. (b) Superluminal case, with $v = 3c$.

Figure 12 plots not only the exact dispersion diagram but also the linear approximation derived in Sec. 5.1. It may be seen that latter coincides with the former as expected.

5.6 Equal-Phase Crystals

The formulas of the previous sections are completely general and readily amenable to computation. For presentation simplicity, the rest of the paper studies the particular design of an equal-phase crystal, which is a generalization of the conventional quarter-stack structure. In this section, we find the closed-form expressions of the average and difference phase of equal-phase crystals.

We define a bilayer equal-phase crystal as a crystal whose two layers constituting the unit cell induce the same round-trip phase shift, i.e.,

$$\bar{\varphi} = \bar{\varphi}_j = \bar{\varphi}_k. \tag{90}$$

For stationary crystals, this corresponds to the condition $n_i\ell_i = n_j\ell_j$, which is called the quarter-wave stack condition when $n_i\ell_i = n_j\ell_j = \lambda_0/4$.[62]

In the subluminal case, the expression of the average phase is written in terms of the lengths, the modulation velocity, and the wave velocities by inserting Eq. (38b) into Eq. (90), yielding

$$\bar{\varphi} = \omega_{\mathrm{e}} \frac{\ell_j v_j}{v_j^2 - v_{\mathrm{m}}^2} = \omega_{\mathrm{e}} \frac{\ell_k v_k}{v_k^2 - v_{\mathrm{m}}^2} = \omega_{\mathrm{e}} d_{\mathrm{e}}/2, \tag{91}$$

where the quantity d_{e} corresponds to the time a wave takes to accomplish a round trip in a layer, as can be found geometrically from the plot of d_{e} in Fig. 9(a). Therefore, if two layers have the same round-trip duration d_{e}, we will call them equal-phase. For later use, we express this round-trip duration in terms of the physical length of the unit cell, ℓ_{B}, as

$$d_{\mathrm{e}} = \frac{2v_j v_k}{(v_j + v_k)(v_j v_k - v_{\mathrm{m}}^2)} \ell_{\mathrm{B}}, \tag{92}$$

which may also be found geometrically from Fig. 9(a).

The total phase difference $\Delta\varphi$ between forward and backward waves in the entire unit-cell is

$$\begin{aligned}\Delta\varphi = \Delta\varphi_j + \Delta\varphi_k &= v_{\mathrm{m}}\gamma^2 \frac{(v_j + v_k)(1 - v_j v_k/c^2)}{v_j v_k} \omega_{\mathrm{e}} d_{\mathrm{e}} \\ &= 2v_{\mathrm{m}}\gamma^2 \frac{1 - v_j v_k/c^2}{v_j v_k - v_{\mathrm{m}}^2} \omega_{\mathrm{e}} \ell_{\mathrm{B}}.\end{aligned} \tag{93}$$

where Eqs. (38c) and (92) have been used in the second and third equalities.

In the superluminal case, the equal-phase condition is written in terms of the durations of the layers, the modulation velocity and the wave velocities by inserting Eq. (41b) into Eq. (90), yielding

$$\bar{\varphi} = k_{\mathrm{e}} \frac{d_j v_{\mathrm{m}}^2 v_j}{v_{\mathrm{m}}^2 - v_j^2} = k_{\mathrm{e}} \frac{d_k v_{\mathrm{m}}^2 v_k}{v_{\mathrm{m}}^2 - v_k^2} = k_{\mathrm{e}} \ell_{\mathrm{e}}/2, \tag{94}$$

where ℓ_{e} corresponds to the total travel length of the forward and backward waves in a slab, as can be found from Fig. 9(b), and is related to the duration d_{B} through

$$\ell_{\mathrm{e}} = \frac{2v_{\mathrm{m}}^2 v_j v_k}{(v_j + v_k)(v_{\mathrm{m}}^2 - v_j v_k)} d_{\mathrm{B}}. \tag{95}$$

The total phase difference, $\Delta\varphi$, is

$$\begin{aligned}\Delta\varphi = \Delta\varphi_j + \Delta\varphi_k &= \gamma^2 \frac{c^2}{v_{\mathrm{m}}^2} \frac{(v_j + v_k)(1 - v_j v_k/c^2)}{v_j v_k} k_{\mathrm{e}} \ell_{\mathrm{e}} \\ &= v_{\mathrm{m}} c^2 \gamma^2 \frac{1 - v_j v_k/c^2}{v_j v_k - v_{\mathrm{m}}^2} k_{\mathrm{e}} d_{\mathrm{B}},\end{aligned} \tag{96}$$

where Eq. (41c) and Eq. (95) have been used in the second and third equalities.

5.7 Description of the Dispersion Diagram

5.7.1 Brillouin zone

The dispersion diagrams corresponding to the exact solutions Eq. (86) and Eq. (89) are plotted only for first Brillouin zones

in Fig. 12 since the rest of the diagrams follows by periodicity. To find the limits of the Brillouin zones, we study Eq. (83), and see that this function is periodic in $\Phi_B - \Delta\varphi = 2\pi n$. We therefore define the Brillouin zones as delimited by

$$\Phi_B - \Delta\varphi = \pm\pi. \tag{97}$$

In the subluminal case, this can be expressed in terms of the frequency and wavenumber by substituting Eqs. (84) and (93) with Eq. (85) into Eq. (97), yielding

$$k = \frac{v_m}{v_j v_k}\omega \pm \frac{\pi(v_j v_k - v_m^2)}{v_j v_k \ell_B}. \tag{98}$$

This is the expression for the two oblique lines delimiting the Brillouin zone. Their slope is $v_j v_k / v_m$, and the k-intercepts are $\pm\pi(v_j v_k - v_m^2)/(v_j v_k \ell_B)$, reducing, as expected, to $\pm\pi/\ell_B$ in the stationary case. Note that the limits of the Brillouin zone are not parallel to the ω' axis, as they would be for the case of a moving medium. In the case of a moving isotropic medium, the crystal would appear stationary in the moving frame and so the Brillouin zone would be parallel to the ω' axis.

In the superluminal case, substituting Eqs. (87) and (96) with Eq. (88) into Eq. (97) yields

$$\omega = \frac{v_j v_k}{v_m} k \pm \frac{\pi(v_m^2 - v_j v_k)}{v_m^2 d_B}, \tag{99}$$

with the slope being again $v_j v_k / v_m$.

5.7.2 Complex nature of the bandgaps

The bandgaps correspond to the imaginary part of the solution in Fig. 12, with the imaginary frequencies alternating along the k axis and the imaginary wavenumbers alternating along the ω axis. We see that the frequencies and the wavenumbers are simultaneously complex, for both the subluminal and superluminal regimes. This is a feature that seems to have been previously overlooked in the literature, although it is a straightforward consequence of the Lorentz transformations.

In the subluminal case, the moving-frame solution has the complex wavenumbers $k' = k'_r + ik'_i$, with k'_r, k'_i the real and imaginary parts, and purely real frequencies so that $\omega'_i = 0$. Applying the frequency Lorentz transformation [Eq. (10)] to the imaginary frequency yields $\omega_i - v_m k_i = 0$, or $\omega_i = v_m k_i$, which shows that the complexity of k_i indeed implies the complexity of ω_i, with ω_i non-negligible for relativistic velocities.

In the superluminal case, the moving-frame solution has the complex wavenumbers $\omega' = \omega'_r + i\omega'_i$, with ω'_r, ω'_i the real and imaginary parts, and purely real wavenumbers so that $k'_i = 0$. Applying the wavenumber Lorentz transformation [Eq. (10)] to the imaginary wavenumber, with $v_f = c^2/v_m$, yields $k_i - (1/v_m)\omega_i = 0$, or $k_i = \omega_i / v_m$ so that the complexity of ω_i implies the complexity of k_i, with k_i decreasing as the modulation velocity increases.

5.7.3 Bandgap edges

We now calculate the edges of the bandgaps, indicated as $\mathrm{BG}^{\pm}_{p,q}$ in Fig. 12, where the subscripts indicate the two modes involved, and the superscript $\pm$ refers to the top and bottom edges. Theses edges are found by analyzing the exact solution Eq. (83), which reduces to

$$\cos(\Phi_B - \Delta\varphi) = \cos^2\bar{\varphi} - \frac{1}{2}\left(\frac{\eta_1}{\eta_2} + \frac{\eta_2}{\eta_1}\right)\sin^2\bar{\varphi}, \tag{100}$$

in the equal-phase case, $\bar{\varphi}_1 = \bar{\varphi}_2 = \bar{\varphi}$ (Sec. 5.6).

The bandgaps correspond to complex Bloch–Floquet phases, and therefore to the right-hand side of Eq. (100) being less than -1. Thus, the bandgap edges occur at the limit

$$\cos^2\bar{\varphi} - \frac{1}{2}\left(\frac{\eta_1}{\eta_2} + \frac{\eta_2}{\eta_1}\right)\sin^2\bar{\varphi} = -1. \tag{101}$$

Applying the trigonometric relation $\sin^2(\bar{\varphi}) = 1 - \cos^2(\bar{\varphi})$ and grouping the cosine terms, we find that the bandgap edge condition reduces to

$$\bar{\varphi} = \arccos\left(\pm\frac{\eta_2 - \eta_1}{\eta_1 + \eta_2}\right) = \arccos(\pm\upsilon) \overset{\upsilon\ll 1}{\approx} \frac{\pi}{2} \mp \upsilon. \tag{102}$$

This condition delimits two curves on which the bandgap edges lie. In addition, the bandgap edges lie on the Brillouin zone limits, as can be seen in Fig. 12. This is found by noting that the inverse cosine of a quantity less than -1 has the form $\pi + ix$ and at the limit is $\pm\pi$. Setting the inverse cosine of the right-hand side of Eq. (100) equal to $\pm\pi$ retrieves Eq. (97).

In the subluminal case, the condition for the bandgap edge may be written in terms of frequency and wavenumber by inserting Eq. (91) with Eq. (85) into Eq. (102) as

$$\omega = v_m k + \frac{1}{d_e}\arccos(\pm\upsilon), \tag{103}$$

which represent the equations of the parallel straight curves, with slope v_m and ω-intercept $1/d_e \arccos(\pm\upsilon)$, that delimit the bandgap. The Brillouin zone limits are written in terms of frequencies and wavenumbers in Eq. (98). Solving this system of equations provides the bandgap edge positions $\mathrm{BG}_{0,-1}$ as

$$\omega^{\pm}_{0,-1} = \frac{1}{\ell_B}[v_m\pi + (v_j + v_k)\arccos(\pm\upsilon)], \tag{104a}$$

$$k^{\pm}_{0,-1} = \frac{1}{\ell_B}\left[\pi + \frac{v_m(v_j + v_k)}{v_j v_k}\arccos(\pm\upsilon)\right]. \tag{104b}$$

From these results, we may express the bandgap width $\Delta\omega_{0,-1} = \omega^{+}_{0,-1} - \omega^{-}_{0,-1}$ as

$$\Delta\omega_{0,-1} = \frac{v_j + v_k}{\ell_B}[\arccos\upsilon - \arccos(-\upsilon)] \overset{\upsilon\ll 1}{\approx} 2\frac{vj + v_k}{\ell_B}|\upsilon|, \tag{105}$$

and the corresponding wavenumber width $\Delta k_{0,-1} = k^{+}_{0,-1} - k^{-}_{0,-1}$, simply found as $\Delta k_{0,-1} = \Delta\omega_{0,-1} v_m/(v_j v_k)$ from the geometrical construction in Fig. 12(a).

Note that the bandgap widths are the same for all the bandgaps in the case of equal-phase crystals so that the edges of all the bandgaps may be found from the bandgap width expressions and the center positions provided in Eq. (65).

In the superluminal case, the bandgap edges lie at the intersection of the straight line given by Eq. (102) and the Brillouin

zone limits, the former of which is rewritten in terms of frequency and wavenumber by inserting Eq. (94) with Eq. (88) into Eq. (102) as

$$k = \frac{\omega}{v_\mathrm{m}} + \frac{1}{\ell_\mathrm{e}} \arccos(\pm\upsilon), \tag{106}$$

and the latter of which corresponds to Eq. (99). Solving for this system of equations, we find the positions of the limits of the gap $\mathrm{BG}_{0,-1}$, denoted by $\mathrm{BG}^{\pm}_{0,-1}$ in Fig. 12(b), as

$$k^{\pm}_{0,-1} = \frac{1}{d_\mathrm{B}}\left[\frac{\pi}{v_\mathrm{m}} + \frac{v_j + v_k}{v_j v_k} \arccos(\pm\upsilon)\right], \tag{107a}$$

$$\omega^{\pm}_{0,-1} = \frac{1}{d_\mathrm{B}}\left[\pi + \frac{v_j + v_k}{v_\mathrm{m}} \arccos(\pm\upsilon)\right]. \tag{107b}$$

From these results, we may express the bandgap width $\Delta k_{0,-1} = k^{+}_{0,-1} - k^{-}_{0,-1}$ as

$$\Delta k_{0,-1} = \frac{v_j + v_k}{v_j v_k d_\mathrm{B}}[\arccos\,\upsilon - \arccos(-\upsilon)] \overset{\upsilon\ll 1}{\approx} 2\frac{v_j + v_k}{v_j v_k d_\mathrm{B}}|\upsilon|, \tag{108}$$

and the frequency width $\Delta\omega_{0,-1} = \omega^{+}_{0,-1} - \omega^{-}_{0,-1}$ is then simply found as $\Delta\omega_{0,-1} = \Delta k_{0,-1} v_j v_k / v_\mathrm{m}$, from the geometrical construction in Fig. 12(b).

6 Truncated Crystal

6.1 Types of Truncation

As for conventional crystals, practical spacetime crystals are necessarily finite and may be truncated along different directions, including now also the time direction.

Figure 13 describes examples of spacetime crystal truncation. In the top row [Figs. 13(a)–13(c)], the crystals are truncated on the left and on the right by interfaces sharing the same velocity. In the bottom row [Figs. 13(d)–13(f)], the crystals are truncated on the left and on the right by interfaces of different velocities. The truncations of Fig. 13 represent only a few of an infinite number of possibilities, including for instance multiple truncations separating the crystal in different parts, truncations delimiting holes, or spacetime defects, in the crystal, or periodic truncation leading to a multiscale spacetime crystal.

Figure 14 shows the scattering phenomenology for truncated spacetime crystals, with Fig. 14(a) corresponding to the comoving structure of Figs. 13(c) and 14(b) corresponding to the purely spatially truncated crystal of Fig. 13(a). The top panels show the frequency transitions in the dispersion diagrams, and the bottom panels show the different scattered waves in the spacetime diagrams.

Let us start with the comoving truncated crystal [Fig. 14(a)]. The transition frequencies are obtained through the following construction. First, we plot the dispersion diagrams of the spacetime crystal (Sec. 5.5) and of the surrounding medium, which is here a simple pair of straight lines in the present nondispersive case. Second, we place the point corresponding to the incident wave, labeled ①, on the dispersion diagram of the incident medium. Third, we trace an oblique line of slope v_m/c,

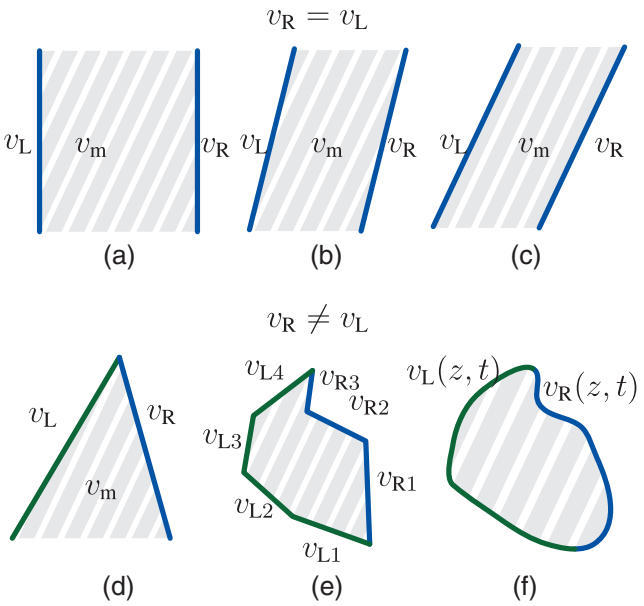

Fig. 13 Examples of spacetime crystal truncation by a pair of spactime interfaces of velocities υ_L and υ_R for the left and right interfaces, respectively. Top row: the two interfaces have the same velocity, $\upsilon_\mathrm{L} = \upsilon_\mathrm{R}$. Bottom row: the two interfaces have different velocities, $\upsilon_\mathrm{L} \neq \upsilon_\mathrm{R}$. (a) Purely spatial truncation, $\upsilon_\mathrm{L} = \upsilon_\mathrm{R} = 0$. (b) Truncation with velocity different from the modulation velocity, $\upsilon_\mathrm{L} = \upsilon_\mathrm{R} \neq \upsilon_\mathrm{m}$. (c) Comoving truncation, $\upsilon_\mathrm{L} = \upsilon_\mathrm{R} = \upsilon_\mathrm{m}$. (d) Antiparallel truncation, $\upsilon_\mathrm{L} \neq \upsilon_\mathrm{R} \neq \upsilon_\mathrm{m}$. (e) Spacetime cavity with piecewise constant velocities. (f) Spacetime cavity with continuously varying velocity.

corresponding to the moving-frame conserved frequency (see Sec. 3.3). The intersections of this line with the two dispersion diagrams provide the scattered frequencies. The corresponding scattered waves are represented in the spacetime diagram below the dispersion diagram.

We notice that, although infinitely many frequencies are excited inside the crystal (solutions labeled ③–⑦), the transmitted and reflected waves are monochromatic. Indeed, in the moving frame, the interfaces appear stationary so that a single frequency exists throughout the structure. Therefore, the reflected and transmitted solutions in the laboratory frame, found by applying the frequency Lorentz transformation [Eq. (10)], are also monochromatic. The incident and transmitted waves both transform in the same way since they both propagate in the same direction, whereas the reflected wave, propagating in the opposite direction, acquires a different frequency. In the case of Fig. 14(a), it is downshifted, as expected from the Doppler effect for a receding structure.

We now proceed to the analysis of the purely spatially truncated crystal [Fig. 14(b)]. The transition frequencies are obtained through the following construction. First, we plot again the dispersion diagrams of the spacetime crystal and the surrounding media, along with the incident wave, labeled ①. Second, we enforce frequency conservation at the first interface by tracing horizontal lines, which leads to the reflected wave labeled ② and the transmitted wave labeled ③. The frequency conservation in the moving frame involves then all the harmonic waves along the oblique line of slope v_m/c (labeled ④–⑦). Due to frequency conservation at the left and

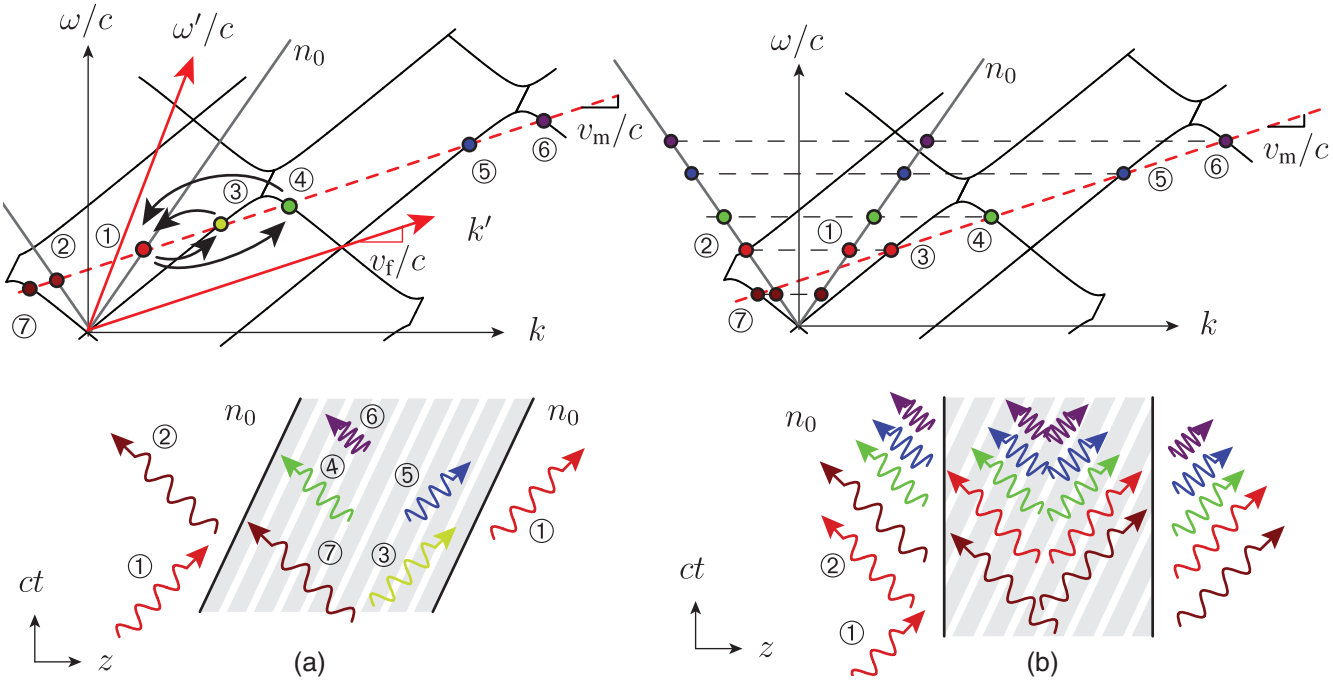

Fig. 14 Scattering from two canonical truncated spacetime crystals. In both cases, the crystal is subluminal, and the medium surrounding it is a simple nondispersive dielectric medium of refractive index n_0. Top row: dispersion diagrams with transition frequencies. Bottom row: spacetime diagrams with scattered waves, with labels corresponding the solutions of the top panels. Note that the drawn scattered waves correspond to the waves seen in the laboratory frame and would completely different in the moving frame. (a) Comoving truncation. A moving-frame observer would see a stationary crystal bounded by stationary interfaces, and hence measure a unique frequency everywhere, inside and outside the crystal. The arrows indicate the up and down frequency and wavenumber transitions at the two interfaces. (b) Purely spatial truncation. A moving-frame observer would see a stationary crystal bounded by moving interfaces, and hence measure an infinity of frequencies.

right interfaces, each of these harmonics produces a corresponding wave in the surrounding medium so that the scattered waves contain multiple harmonics.

6.2 Scattering Coefficients

We now apply the transfer matrix technique to solve the problem of the comoving truncation spacetime crystal [Fig. 14(a)]. The spatially truncated spacetime crystal may be studied using conventional phase matching and Bloch–Floquet techniques.[6,39]

The transmission and reflection coefficients of a spacetime crystal truncated by comoving interfaces of N periods may be obtained by simply multiplying unit-cell transfer matrix Eq. (78) N times and then extracting the coefficients. An alternative approach to the matrix multiplication is the application of the Chebyshev identity[62]

$$[M_{\mathrm{B}}]^N = \mathrm{e}^{iN\Delta\phi}[M_{\mathrm{B}0}] = \mathrm{e}^{iN\Delta\phi}\begin{bmatrix} a\mathcal{U}_{N-1}(x)-\mathcal{U}_{N-2}(x) & ib\mathcal{U}_{N-1}(x) \\ ic\mathcal{U}_{N-1}(x) & a^*\mathcal{U}_{N-1}(x)-\mathcal{U}_{N-2}(x) \end{bmatrix}, \tag{109}$$

where $\mathcal{U}_N$ are the Chebyshev polynomials of the second kind, defined as

$$\mathcal{U}_N(x) = \frac{\sin[(N+1)\cos^{-1}x]}{\sqrt{1-x^2}}, \tag{110}$$

with the argument

$$x = \frac{a+a^*}{2}, \tag{111}$$

where we recall that a, a^*, b, and c are the elements of the unit-cell matrix M_{B}, given in Eqs. (79).

To extract the total transmission and reflection coefficients, the scattering matrix is written in terms of transfer-matrix parameters:

$$\begin{bmatrix} \psi_1^- \\ \psi_N^- \end{bmatrix} = \begin{bmatrix} \Gamma_{11} & \overline{T}_{1N} \\ T_{N1} & \overline{\Gamma}_{NN} \end{bmatrix}\begin{bmatrix} \psi_1^+ \\ \psi_N^+ \end{bmatrix} = \frac{1}{A^*}\begin{bmatrix} -A & 1 \\ AA^*-BC & A \end{bmatrix}\begin{bmatrix} \psi_1^+ \\ \psi_N^+ \end{bmatrix}, \tag{112}$$

with A, A^*, B, C corresponding to the a, a^*, b, c elements of the $[M_{\mathrm{B}}]^N$ matrix.

The results are plotted in Fig. 15(a). We notice for waves in the gap, the reflected wave is partly absorbed by the structure since the reflection coefficient is less than one, and there is no transmitted wave.

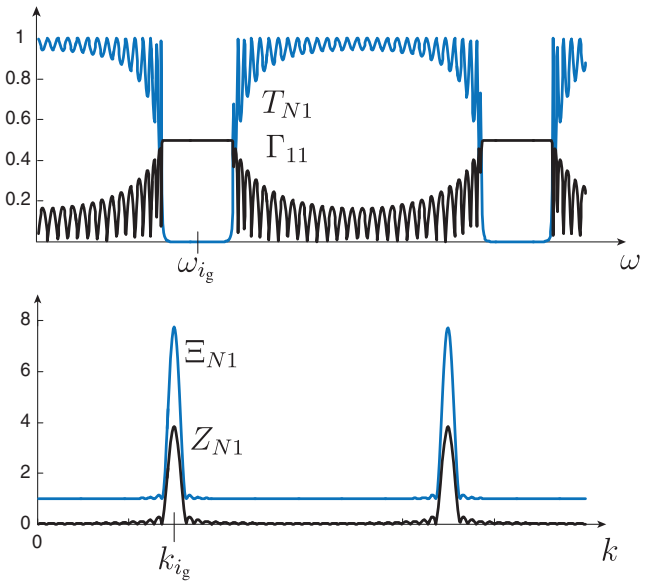

Fig. 15 Transmission and reflection coefficients for an $N = 15$-layer crystal [corresponding to Fig. 13(c) and Fig. 14(a)] with $\bar{\phi}_{1,2} = \pi/2$. The gap centers ω_i, k_i are provided in Appendix E (Sec. 12). (a) Subluminal case, with $v = 1/3c$ and $n_2/n_1 = 2$, with attenuation in the bandgaps. (b) Superluminal case, with $v = 3c$ and $n_2/n_1 = 1.2$ with amplification in the bandgaps.

For the superluminal crystal, the scattering matrix is the same as the transfer matrix since waves in the last medium are also the scattered waves. The coefficients are thus

$$Z_{N1} = A, \tag{113a}$$

$$\Xi_{N1} = C, \tag{113b}$$

and are plotted in Fig. 15. We see that in the gap, both the transmitted and the reflected waves are amplified. This is consistent with the analysis of the interference for a superluminal slab in Sec. 4: both scattered waves are in constructive interference in the bandgap.

We note that the bandgap centers in Fig. 15 do not correspond to the bandgap centers calculated in Eqs. (65) and (67). This is due to the effect shown in Fig. 14(a): the frequencies horizontally aligned with the bandgaps will not see the bandgap. Instead, the frequencies aligned on an oblique line of slope v_m and passing through the bandgap will see the bandgap. The bandgap centers of Fig. 15 are provided in Appendix E (Sec. 12).

7 Conclusion

We have performed a comprehensive analysis of uniform-velocity bilayer spacetime crystals. We started with the problem of spacetime interfaces, then addressed the problem of double-interfaces, or spacetime slabs, next solved the problem of unbounded crystals, and finally studied the problem of truncated crystals.

Throughout the paper, we have made extensive use of special relativity concepts, including the graphical tool of spacetime diagrams, which offered remarkable resolution simplicity, provided deep insight into the physics, and led us to uncover a number of new results. The new insights include a vivid Bragg-type description of the bandgap interference phenomenology, a quick linear approximation of dispersion diagrams, and the explanation of the effect of the truncation. The new results include the generalization of the Stokes principle to spacetime interfaces and the description of the simultaneous frequency and wavenumber complexity in the bandgaps.

This work may be extended to multilayer-cell spacetime crystals, spacetime crystals made of dispersive media, and higher dimension crystals.

8 Appendix A: Bianisotropy, Wave Impedance, and Wave Velocity in the Moving Frame

We derive here the constitutive relations for homogeneous isotropic media as seen in a moving frame. Figure 16 represents a modulated spacetime interface, from the viewpoint of the laboratory frame in Fig. 16(a) and from the viewpoint of the moving frame in Fig. 16(b). In Fig. 16(a), the interface of the spacetime modulation moves to the right but its constitutive particles have vertical trajectories, i.e., appear stationary. In Fig. 16(b), the interface appears stationary, but the particles appear in motion, moving to the left.

We first write the constitutive relations of the bulk stationary medium in the laboratory frame

$$D_{xj} = \epsilon_j E_{xj}, \tag{114a}$$

$$B_{yj} = \mu_j H_{yj}. \tag{114b}$$

Applying the Lorentz transformations [Eq. (13)] to these relations yields

$$D'_{xj} - \frac{v_f}{c^2} H'_{yj} = \epsilon_j (E'_{xj} - v_f B'_{yj}), \tag{115a}$$

and

$$B'_{yj} - \frac{v_f}{c^2} E'_{xj} = \mu_j (H'_{yj} - v_f D'_{xj}). \tag{115b}$$

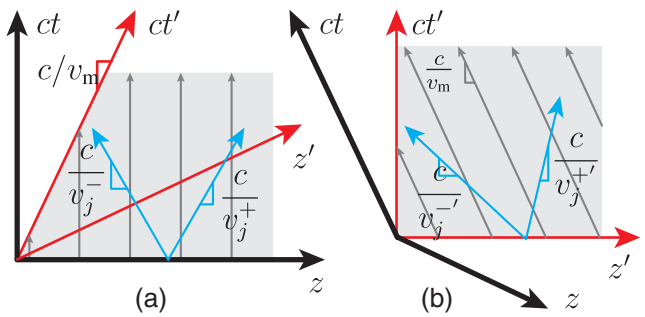

Fig. 16 Spacetime interface represented in two inertial frames. The arrows represent the trajectories of the media particles. In both (a) and (b), the interfaces of the spacetime variation are parallel to the ct' axis and the media trajectories are parallel to the ct axis. (a) Laboratory frame viewpoint. Media appear at rest. Wave velocity is independent of direction: $v_j^+ = v_j^-$ (b) Moving frame viewpoint. Media appear to be moving in $-z$ direction. Wave velocities are direction dependent: $v_j^+ \neq v_j^-$, with $|v_j^-| > |v_j^+|$.

Solving Eqs. (115a) and (115b) for D_y' and B_x', we obtain the constitutive relations

$$D_{xj}' = \epsilon_j \frac{1-v_f^2/c^2}{1-v_f^2/v_j^2} E_{xj}' + \frac{v_f}{c^2}\frac{1-c^2/v_j^2}{1-v_f^2/v_j^2} H_{yj}' = \epsilon_j' E_{xj}' + \chi_j' H_{yj}', \tag{116a}$$

and

$$B_{yj}' = \mu_j \frac{1-v_f^2/c^2}{1-v_f^2/v_j^2} H_{yj}' + \frac{v_f}{c^2}\frac{1-c^2/v_j^2}{1-v_f^2/v_j^2} E_{xj}' = \mu_j' H_{yj}' + \chi_j' E_{xj}', \tag{116b}$$

where v_j is the velocity of light in the medium in the laboratory frame, $v_j = 1/\sqrt{\epsilon_j \mu_j}$. These equations reveal that the medium is biisotropic in the moving frame, since the magnetoelectric coupling terms are scalar, and, more specifically, a Tellegen medium, since the there is a unique variable χ_j for both the electromagnetic and the magnetoelectric coupling terms. More generally, moving volumes appear bianisotropic in the moving frame. Indeed, the media do not transform the same way in the directions parallel and perpendicular to the motion of the medium.

We next calculate the wave impedance and the wave velocity of moving isotropic media. We first write the Maxwell curl equations for a plane monochromatic wave:

$$\omega_j' D_{xj}' = k_j' H_{yj}', \quad \omega_j' B_{yj}' = k_j' E_{xj}'. \tag{117}$$

Dividing the left equation of Eq. (117) by the right equation of Eq. (117), we find

$$\frac{D_{xj}'}{H_{yj}'} = \frac{B_{yj}'}{E_{xj}'}. \tag{118}$$

Inserting the constitutive relations [Eq. (116b)] into Eq. (118), we find the impedance η_j', defined as the ratio of the E and H fields:

$$\eta_j' = \frac{E_{xj}'}{H_{yj}'} = \sqrt{\frac{\mu_j'}{\epsilon_j'}} = \sqrt{\frac{\mu_j}{\epsilon_j}} = \eta_j, \tag{119}$$

where the third equality comes from the definitions of μ', ϵ' in Eqs. (116). We thus conclude from Eq. (119) that the impedance is invariant under a change of frames.

The wave velocity, defined as $v_j^{\pm'} = \omega_j'/k_j'$, is found from Eq. (117) as

$$v_j^{\pm'} = \frac{\omega_j'}{k_j'} = \frac{H_{yj}'}{D_{xj}'} = \frac{E_{xj}'}{B_{yj}'}, \tag{120}$$

inserting Eqs. (119) and (116) into Eq. (120) yields

$$v_j^{\pm'} = \frac{H_{yj}'}{D_{xj}'} = \frac{1}{\epsilon_j'\eta_j' + \chi_j'} = \frac{v_j^{\pm} + v_f}{1 + v_j^{\pm} v_f/c^2}. \tag{121}$$

Comparing this result with the addition law of velocities provided in Eq. (7b), we see a sign difference of v_f, due to the fact that for a positive modulation velocity, $v_m > 0$, the medium appear to be moving in the $-z'$ direction in the moving frame, as drawn in Fig. 16(b).

9 Appendix B: Alternative Derivation of the Continuity Conditions

We start with 1-D Maxwell equations,

$$\frac{\partial E_x}{\partial z} = -\frac{\partial B_y}{\partial t} = -\frac{\partial \mu(z - v_m t) H_y}{\partial t}, \tag{122a}$$

$$\frac{\partial H_y}{\partial z} = -\frac{\partial D_x}{\partial t} = -\frac{\partial \epsilon(z - v_m t) E_x}{\partial t}, \tag{122b}$$

and apply the following coordinate transformation:

$$z' = z - v_m t, \quad t' = t. \tag{123}$$

This does not correspond to a Lorentz transformation and, therefore, does not lead to invariance. The partial derivatives of Eq. (122) are found as

$$\frac{\partial}{\partial z} = \frac{\partial}{\partial z'}\frac{\partial z'}{\partial z} + \frac{\partial}{\partial t'}\frac{\partial t'}{\partial z} = \frac{\partial}{\partial z'}, \tag{124a}$$

$$\frac{\partial}{\partial t} = \frac{\partial}{\partial t'}\frac{\partial t'}{\partial t} + \frac{\partial}{\partial z'}\frac{\partial z'}{\partial t} = \frac{\partial}{\partial t'} - v_m \frac{\partial}{\partial z'}. \tag{124b}$$

Substituting these relations into Eq. (122) yields

$$\frac{\partial E_x}{\partial z'} = -\left(\frac{\partial}{\partial t'} - v_m \frac{\partial}{\partial z'}\right)\mu(z') H_y, \tag{125a}$$

$$\frac{\partial H_y}{\partial z'} = -\left(\frac{\partial}{\partial t'} - v_m \frac{\partial}{\partial z'}\right)\epsilon(z') E_x. \tag{125b}$$

Rearranging Eq. (125), we find

$$\frac{\partial}{\partial z'}[E_x - v_m \mu(z') H_y] = -\frac{\partial}{\partial t'}\mu(z') H_y, \tag{126a}$$

$$\frac{\partial}{\partial z'}[H_y - v_m \epsilon(z') E_x] = -\frac{\partial}{\partial t'}\epsilon(z') E_x. \tag{126b}$$

Inspecting these equations, we can deduce the continuity conditions by reasoning ad absurbdum: if the arguments of the $\partial z'$ derivative on the left-hand side in Eq. (126), $E_x + v_m \mu(z') H_y$ or $H_y + v_m \epsilon(z') E_x$, vary as a step function, then the right-hand side would be an impulse function, which is unphysical. Therefore, quantities $E_x + v_m \mu(z') H_y$ and $H_y + v_m \epsilon(z') E_x$, or $E_x + v_m B_y$ and $H_y + v_m D_x$, must be continuous at the interface. We can see that in the limiting case when $v_m = 0$, the quantities E_x, H_y are continuous, as expected. In the limiting case $v_m = \infty$, the quantities D_x, B_y are continuous, as reported in Ref. 59.

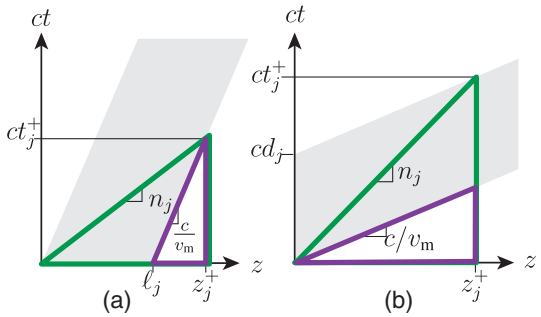

Fig. 17 Graphical derivation of the travel length or duration across the unit cell of the crystal. (a) Subluminal regime (length). (b) Superluminal regime (duration).

10 Appendix C: Travel Length or Duration Across a Slab

Consider Fig. 17. Each graph involves two triangles, one with slope n_j and the other with slope c/v_m.

In the subluminal case, represented in Fig. 17(a), we have

$$n_j = \frac{ct_j^+}{z_j^+}, \quad \frac{c}{v_m} = \frac{ct_j^+}{z_j^+ - \ell_j}. \tag{127}$$

Isolating z_j^+ in both relations

$$z_j^+ = \frac{ct_j^+}{n_j}, \quad z_j^+ = \ell_j + ct_j^+ \frac{v_m}{c}, \tag{128}$$

and equating these results yields

$$\frac{ct_j^+}{n_j} = \ell_j + ct_j^+ \frac{v_m}{c}, \quad t_j^+ = \frac{\ell_j n_j / c}{1 - v_m n_j / c}. \tag{129}$$

Similarly, in superluminal case, represented in Fig. 17(b), we have

$$n_j = \frac{ct_j^+}{z_j^+}, \quad \frac{c}{v_m} = \frac{ct_j^+ - cd_j}{z_j^+}. \tag{130}$$

Isolating ct_j^+ in both relations

$$ct_j^+ = z_j^+ n_j, \quad ct_j^+ = \frac{c}{v_m} z_j^+ + cd_j, \tag{131}$$

and equating these results yields

$$z_j^+ n_j = \frac{c}{v_m} z_j^+ + cd_j, \quad z_j^+ = \frac{cd_j}{n_j - c/v_m}. \tag{132}$$

11 Appendix D: Unit-Cell Matrix Symmetry

We deduce the properties of the unit-cell transfer matrix

$$\begin{bmatrix} \psi_{out}^+ \\ \psi_{out}^- \end{bmatrix} = [M_B] \begin{bmatrix} \psi_{in}^+ \\ \psi_{in}^- \end{bmatrix}, \tag{133}$$

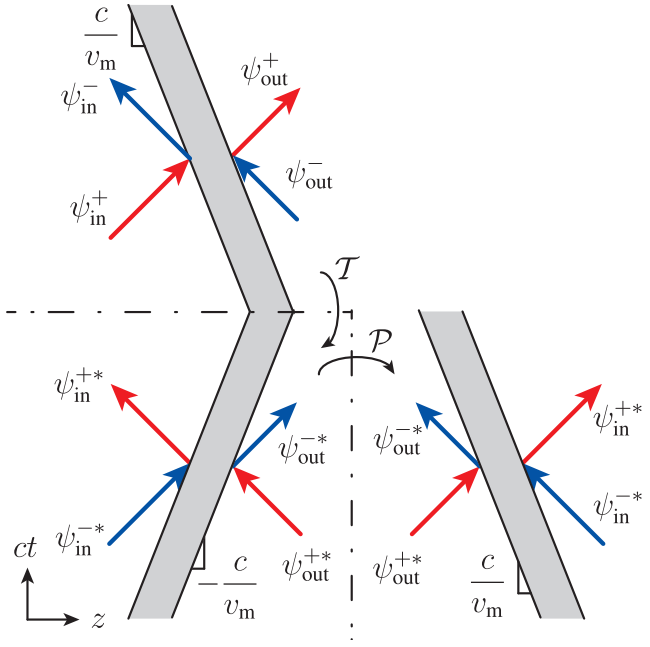

Fig. 18 Successive application of time reversal (T) and space reversal (P).

by applying a spacetime symmetry argument, with the help of Fig. 18. The initial problem of a spacetime slab is represented in the top left panel of the figure. A time reversal and a space reversal are successively applied to this problem, resulting in the bottom right panel, which retrieves the initial problem. We therefore expect the matrix relating the fields on the left to the fields on the right of the slab to be the same for the spacetime reversed problem and for the initial problem. According to the bottom right panel of Fig. 18

$$\begin{bmatrix} \psi_{in}^{+*} \\ \psi_{in}^{-*} \end{bmatrix} = [M_B] \begin{bmatrix} \psi_{out}^{+*} \\ \psi_{out}^{-*} \end{bmatrix}. \tag{134}$$

Taking the complex conjugate of this relation and multiplying the resulting equation by the inverse of M_B^* reveals the following property:

$$[M_B^*]^{-1} = M_B, \tag{135}$$

or, in terms of the matrix elements

$$\begin{bmatrix} a & b \\ c & d \end{bmatrix} = \frac{1}{\det[M]} \begin{bmatrix} d^* & -b^* \\ -c^* & a^* \end{bmatrix}. \tag{136}$$

Since for spacetime slab, $\det[M_B] = e^{i\Delta\phi}$ (see Sec. 5.3)

$$a e^{i\Delta\phi} = d^*, \tag{137}$$

$$b e^{i\Delta\phi} = -b^*, \quad c e^{i\Delta\phi} = -c^* \tag{138}$$

which is consistent with the results in Ref. 68 and with Eq. (79) of Sec. 5.3.

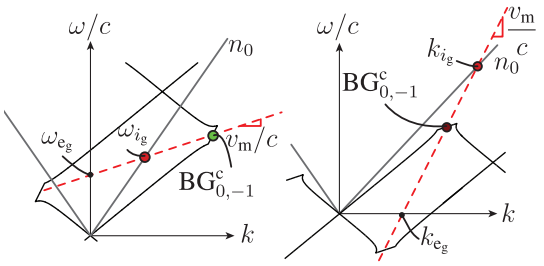

Fig. 19 Construction to find the frequencies aligned with the bandgaps. (a) Subluminal regime. (b) Superluminal regime.

12 Appendix E: Frequency Centers for Parallel Truncation

Here, we calculate the incident frequencies and wavenumbers aligned with the bandgaps in the case of a comoving truncation. Figure 19 provides the graphical construction, with the dispersion of the incident medium of refractive index n_0 and the dispersion diagram of the spacetime crystals.

We start with the subluminal case. We first deduce ω_{e_g}, which is found from Fig. 19(a) to satisfy

$$\omega_{e_g} = \omega^c_{0,-1} - v_m k^c_{0,-1} = (v^+_{av} - v_m)\frac{v_m + v^-_{av}}{v^+_{av} + v^-_{av}} k_B, \tag{139a}$$

where the expressions for the bandgap centers of Eq. (65) in the paper were used. The incident frequencies aligned with the center of the bandgap, ω_{i_g}, are expressed as a function of ω_{e_g} as

$$\omega_{i_g} = \frac{v_i}{v_i - v_m}\omega_{e_g}. \tag{139b}$$

Similarly, in the superluminal case, k_{e_g} is found from Fig. 19(b) as

$$k_{e_g} = k^c_{0,-1} - \frac{\omega^c_{0,-1}}{v_m} = \left(\frac{1}{v^+_{av}} - \frac{1}{v_m}\right)\frac{v^+_{av}}{v_m}\frac{v^-_{av} + v_m}{v^-_{av} + v^+_{av}}\omega_B, \tag{140a}$$

where the bandgap center expressions of Eq. (67) in the paper were used for the second equality. The incident wavenumbers aligned with the center of the bandgap, k_{i_g}, are expressed as a function of k_{e_g} as

$$k_{i_g} = \frac{v_m}{v_m - v_i}k_{e_g}. \tag{140b}$$

References

1. N. Ashcroft and N. Mermin, *Introduction to Solid State Physics*, Saunders, Philadelphia (1976).
2. J. D. Joannopoulos et al., *Photonic Crystals: Molding the Flow of Light*, Princeton University Press, Princeton/Oxford (2011).
3. B. E. A. Saleh and M. C. Teich, *Fundamentals of Photonics*, Wiley, New Jersey (2007).
4. W. H. Bragg and W. L. Bragg, "The reflection of x-rays by crystals," *Proc. R. Soc. Lond. A.* **88**(605), 428–438 (1913).
5. D. Holberg and K. Kunz, "Parametric properties of fields in a slab of time-varying permittivity," *IEEE Trans. Antennas Propag.* **14**(2), 183–194 (1966).
6. R. Fante, "Transmission of electromagnetic waves into time-varying media," *IEEE Trans. Antennas Propag.* **19**(3), 417–424 (1971).
7. A. Kamal, "A parametric device as a nonreciprocal element," *Proc. IRE* **48**(8), 1424–1430 (1960).
8. L. Baldwin, "Nonreciprocal parametric amplifier circuits," *Proc. IRE* **49**(6), 1075–1101 (1961).
9. J. R. Zurita-Sánchez, P. Halevi, and J. C. Cervantes-González, "Reflection and transmission of a wave incident on a slab with a time-periodic dielectric function ε(t)," *Phys. Rev. A* **79**, 053821 (2009).
10. J. Vila et al., "A Bloch-based procedure for dispersion analysis of lattices with periodic time-varying properties," *J. Sound Vibr.* **406**, 363–377 (2017).
11. T. Koutserimpas and R. Fleury, "Electromagnetic waves in a time periodic medium with step-varying refractive index," *IEEE Trans. Antennas. Propag.* **66**(10), 5300–5307 (2018).
12. E. Lustig, Y. Sharabi, and M. Segev, "Topological aspects of photonic time crystals," *Optica* **5**(11), 1390–1395 (2018).
13. K. Giergiel et al., "Topological time crystals," *New J. Phys.* **21**(11), 052003 (2019).
14. D. K. Kalluri, *Electromagnetics of Time Varying Complex Media: Frequency and Polarization Transformer*, CRC Press, Florida (2010).
15. A. Shlivinski and Y. Hadad, "Beyond the Bode–Fano bound: wideband impedance matching for short pulses using temporal switching of transmission-line parameters," *Phys. Rev. Lett.* **121**(20), 204301 (2018).
16. M. Mirmoosa et al., "Time-varying reactive elements for extreme accumulation of electromagnetic energy," *Phys. Rev. Appl.* **11**(1), 014024 (2019).
17. A. Shapere and F. Wilczek, "Classical time crystals," *Phys. Rev. Lett.* **109**(16), 160402 (2012).
18. M. Skorobogatiy and J. D. Joannopoulos, "Rigid vibrations of a photonic crystal and induced interband transitions," *Phys. Rev. B* **61**(8), 5293–5302 (2000).
19. M. Skorobogatiy and J. D. Joannopoulos, "Photon modes in photonic crystals undergoing rigid vibrations and rotations," *Phys. Rev. B* **61**(23), 15554–15557 (2000).
20. H. Qu et al., "Frequency generation in moving photonic crystals," *J. Opt. Soc. Am. B* **33**(8), 1616–1626 (2016).
21. D.-W. Wang et al., "Optical diode made from a moving photonic crystal," *Phys. Rev. Lett.* **110**(9), 093901 (2013).
22. C. Doppler, *Über das farbige Licht der Doppelsterne und einiger anderer Gestirne des Himmels*, Königl. Böhm. Society of Sciences, Prague (1842).
23. J. Ramasastry, "Wave interaction with moving boundaries," *Electron. Lett.* **3**(11), 479–481 (1967).
24. C. Tsai and B. Auld, "Wave interactions with moving boundaries," *J. Appl. Phys.* **38**(5), 2106–2115 (1967).
25. J. Bradley, "IV. A letter from the Reverend Mr. James Bradley Savilian Professor of Astronomy at Oxford, and FRS to Dr. Edmond Halley Astronom. Reg. &c. giving an account of a new discovered motion of the fix'd stars," *Philos. Trans. R. Soc.* **35**(406), 637–661 (1729).
26. A. M. Shaltout, V. M. Shalaev, and M. L. Brongersma, "Spatiotemporal light control with active metasurfaces," *Science* **364**(6441), 1–10 (2019).
27. C. Caloz and Z.-L. Deck-Léger, "Spacetime metamaterials," *IEEE Trans. Antennas Propag.*, in review (2019).
28. K. Lurie and S. Weekes, "Wave propagation and energy exchange in a spatio-temporal material composite with rectangular microstructure," *J. Math. Anal. Appl.* **314**(1), 286–310 (2006).
29. K. Lurie, D. Onofrei, and S. Weekes, "Mathematical analysis of the waves propagation through a rectangular material structure in space–time," *J. Math. Anal. Appl.* **355**(1), 180–194 (2009).
30. G. Milton and O. Mattei, "Field patterns: a new mathematical object," *Proc. R. Soc. A* **473**(2198), 20160819 (2017).

31. O. Mattei and G. Milton, "Field patterns without blow up," *New J. Phys.* **19**(9), 093022 (2017).
32. O. Mattei and G. Milton, "Field patterns: a new type of wave with infinitely degenerate band structure," *EPL* **120**(5), 54003 (2018).
33. P. K. Tien, "Parametric amplification and frequency mixing in propagating circuits," *J. Appl. Phys.* **29**(9), 1347–1357 (1958).
34. J. R. Pierce, "Use of the principles of conservation of energy and momentum in connection with the operation of wave-type parametric amplifiers," *J. Appl. Phys.* **30**(9), 1341–1346 (1959).
35. A. Cullen, "A travelling-wave parametric amplifier," *Nature* **181**(4605), 332–332 (1958).
36. Z. Yu and S. Fan, "Complete optical isolation created by indirect interband photonic transitions," *Nat. Photonics* **3**(2), 91–94 (2009).
37. A. Bahabad, M. M. Murnane, and H. C. Kapteyn, "Quasi-phase-matching of momentum and energy in nonlinear optical processes," *Nat. Photonics* **4**(8), 570–575 (2010).
38. S. Taravati, N. Chamanara, and C. Caloz, "Nonreciprocal electromagnetic scattering from a periodically space-time modulated slab and application to a quasisonic isolator," *Phys. Rev. B* **65**(2), 442–452 (2017).
39. N. Chamanara et al., "Optical isolation based on space-time engineered asymmetric photonic band gaps," *Phys. Rev. B* **96**(15), 155409 (2017).
40. C. Caloz et al., "Electromagnetic nonreciprocity," *Phys. Rev. Appl.* **10**(4), 047001 (2018).
41. C. Caloz and A. Alù, "Guest editorial special cluster on magnetless nonreciprocity in electromagnetics," *IEEE Antennas Wirel. Propag. Lett.* **17**(11), 1931–1937 (2018).
42. E. S. Cassedy and A. A. Oliner, "Dispersion relations in time-space periodic media: part I—stable interactions," *Proc. IEEE* **51**(10), 1342–1359 (1963).
43. E. S. Cassedy, "Dispersion relations in time-space periodic media: part II—unstable interactions," *Proc. IEEE* **55**(7), 1154–1168 (1967).
44. F. Biancalana et al., "Dynamics of light propagation in spatiotemporal dielectric structures," *Phys. Rev. E* **75**(4), 046607 (2007).
45. L. Felsen and G. M. Whitman, "Wave propagation in time-varying media," *IEEE Trans. Antennas Propag.* **18**(2), 242–253 (1970).
46. A. B. Shvartsburg, "Optics of nonstationary media," *Phys.-Usp.* **48**(8), 797–823 (2005).
47. J. D. Jackson, *Classical Electrodynamics*, Wiley, New Jersey (1999).
48. L. A. Ostrovskii, "Some 'moving boundary paradoxes' in electrodynamics," *Sov. Phys. Usp.* **18**(6), 452–458 (1975).
49. L.-Q. Shui et al., "One-dimensional linear elastic waves at moving property interface," *Wave Motion* **51**(7), 1179–1192 (2014).
50. Z.-L. Deck-Léger and C. Caloz, "Scattering at interluminal interface," in *IEEE AP-S Int. Antennas Propag.*, IEEE, pp. 165–166 (2018).
51. H. Lorentz, "Electromagnetic phenomena in a system moving with any velocity smaller than that of light," in *Collect. Pap.*, Springer, pp. 172–197 (1937).
52. W. Pauli, *Theory of Relativity*, Courier Corporation, London (1981).
53. A. Einstein, "Zur elektrodynamik bewegter Körper," *Ann. Phys.* **322**(10), 891–921 (1905).
54. H. A. Lorentz et al., *The Principle of Relativity: A Collection of Original Memoirs on the Special and General Theory of Relativity*, Dover Publications, New York (1952).
55. M. Laue, "Die Mitführung des Lichtes durch bewegte Köper nach dem Relativitäts-prinzip," *Ann. Phys.* **328**(10), 989–990 (1907).
56. H. Fizeau, "Sur les hypothèses relatives à l'éther lumineux, et sur une expérience qui parait démontrer que le mouvement des corps change la vitesse avec laquelle la lumière se propage dans leur intérieur," *C.R. Acad. Sci.* **33**, 349 (1851).
57. J. A. Kong, *Electromagnetic Wave Theory*, 7th ed., EMW Publication, New York (2008).
58. Z.-L. Deck-Léger, A. Akbarzadeh, and C. Caloz, "Wave deflection and shifted refocusing in a medium modulated by a superluminal rectangular pulse," *Phys. Rev. B* **97**(10), 104305 (2018).
59. F. R. Morgenthaler, "Velocity modulation of electromagnetic waves," *IEEE Trans. Microwave Theory Tech.* **6**(2), 167–172 (1958).
60. G. Stokes, *Mathematical and Physical Papers*, Vol. **2**, pp. 89–103, Cambridge University Press, New York (2009).
61. V. Bacot et al., "Time reversal and holography with spacetime transformations," *Nat. Phys.* **12**(10), 972–977 (2016).
62. M. Born and E. Wolf, *Principles of Optics*, Cambridge University Press, Cambridge (1980).
63. D. R. Smith and D. Schurig, "Electromagnetic wave propagation in media with indefinite permittivity and permeability tensors," *Phys. Rev. Lett.* **90**(7), 077405 (2003).
64. S. Seshadri, "Asymptotic theory of mode coupling in a space-time periodic medium-Part I: stable interactions," *Proc. IEEE* **65**(7), 996–1004 (1977).
65. S. Elnaggar and G. Milford, "Controlling nonreciprocity using enhanced Brillouin scattering," *IEEE Trans. Antennas Propag.* **66**(7), 3500–3511 (2018).
66. S. Seshadri, "Asymptotic theory of mode coupling in a space-time periodic medium—part II: unstable interactions," *Proc. IEEE* **65**(10), 1459–1469 (1977).
67. F. Abelès, "La théorie générale des couches minces," *J. Phys. Radium* **11**(7), 307–309 (1950).
68. S. Longhi, "$\mathcal{PT}$-symmetric laser absorber," *Phys. Rev. A* **82**, 031801 (2010).

Zoé-Lise Deck-Léger is a PhD student in electrical engineering at Polytechnique Montréal, Canada, where she received her MSc degree in 2017. Her work has mostly been devoted to spacetime problems.

Nima Chamanara received his PhD in electrical engineering from Polytechnique Montréal, Montréal, QC, Canada, in 2015. From 2015 to 2018, he was a postdoctoral fellow with Polytechnique Montréal. Currently, he is a postdoctoral fellow with the Physics Department, McGill University, Montréal. His research interests include computational electromagnetics and multiphysics, metamaterials and metasurfaces, nanophotonics, graphene, and 2-D materials.

Maksim Skorobogatiy has graduated from MIT with PhD in physics in 2001 and MSc in electrical engineering. Since 2003 he is a full professor at Polytechnique Montréal, Canada and he holds a Tier 1 Canada Research Chair in ubiquitous THz photonics. In 2017 he was elevated to fellow of the Optical Society of America for his pioneering contributions to the development of micro structured and photonic crystal multi-material fibers.

Mário G. Silveirinha is a professor of electrical engineering at Instituto Superior Técnico, University of Lisbon, and a Senior Researcher at Instituto de Telecomunicações in Portugal. He is an IEEE fellow since 2014 and the 2018 recipient of the IET Harvey Engineering Research Prize. His current research interests include electromagnetism, plasmonics and metamaterials, quantum optics, and topological effects.

Christophe Caloz received his PhD from École Polytechnique Fédérale de Lausanne in 2000. He was next a postdoctoral fellow at University of California at Los Angeles for 4 years. From 2004 to 2019, he has been a professor and Canada Research Chair at Polytechnique Montréal, and will join Katholieke Universiteit Leuven in January 2020. He has published over 750 technical papers and 20 books and book chapters. His main research has been on metamaterials.